

Extra neutral scalars with vectorlike fermions at the LHCShrihari Gopalakrishna,^{*} Tuhin Subhra Mukherjee,[†] and Soumya Sadhukhan[‡]*Institute of Mathematical Sciences (IMSc), CIT Campus, Taramani, Chennai 600113, India*

(Received 24 April 2015; revised manuscript received 13 January 2016; published 2 March 2016)

Many theories beyond the standard model (BSM) contain new CP -odd and CP -even neutral scalars $\phi = \{A, H\}$, and new vectorlike fermions (ψ_{VL}). The couplings of the CP -odd scalar A to two standard model (SM) gauge bosons cannot occur from renormalizable operators in a CP -conserving sector, but can be induced at the quantum loop level. We compute these effective couplings at the 1-loop level induced by the SM fermions and vectorlike fermions, present analytical expressions for them, and plot them numerically. Using the 8 TeV Large Hadron Collider (LHC) $\gamma\gamma$, $\tau^+\tau^-$ and $t\bar{t}$ channel data, we derive constraints on the effective couplings of the ϕ to standard model gauge bosons and fermions. We present the gluon-fusion channel cross sections of the ϕ at the 8 and 14 TeV LHC, and its branching ratios into SM fermion and gauge-boson pairs. We first present our results in a model independent manner, and then we provide results for some simple models containing ϕ and ψ_{VL} in the singlet and doublet representations of $SU(2)$. In the doublet case, we focus on the two-Higgs-doublet (2HDM) Type-II and Type-X models in the alignment limit.

DOI: 10.1103/PhysRevD.93.055004

I. INTRODUCTION

A long series of experiments culminating in the Large Hadron Collider (LHC) discovery of the Higgs boson at a mass of about 125 GeV has firmly established the standard model (SM) as the correct description of nature up to an energy scale of a few hundred GeV. With this discovery, the theoretical puzzle as to why the Higgs boson remains this light when quantum effects should correct it to the highest scales present in the theory (such as the Planck scale) comes to the fore. This problem of the stability of the electroweak (EW) scale is the well-known hierarchy problem of the SM. This could be a clue that some new physics beyond the standard model (BSM) is present near the EW scale which renders it stable against quantum corrections, making it natural. Many theoretical proposals have been made for this new physics (for reviews see Ref. [1]), and they usually contain new particles at the TeV energy scale. We are poised at a very interesting time when the LHC is probing this energy scale and can tell us if one of these proposals is realized in nature.

Among the possibilities of BSM physics that makes the EW scale natural are models in which the Higgs doublet of the SM is a pseudo-Nambu-Goldstone boson (PNGB). Concrete realizations of this idea, for example, are in models of little Higgs, composite Higgs and extra dimensions (for reviews see Refs. [2–4] respectively). In such models, in addition to the CP -even Higgs boson, there could be new CP -odd scalar (A) and CP -even scalar (H), which we denote collectively as $\phi = \{A, H\}$, that are also

PNGBs due to which their mass is much lower than the cutoff scale. Also, new heavy vectorlike fermions (VLFs, denoted as ψ_{VL}) are usually required, that along with the SM fermions (SMFs) complete some representation of a bigger group containing $SU(2) \otimes U(1)$. The new vectorlike fermions can include vectorlike quarks (VLQs) and vectorlike leptons (VLLs) and may be present in addition to the usual SM quarks (SMQs) and leptons (SMLs). By vectorlike fermions we mean that fermions in a representation of the SM gauge group and in its conjugate representation both appear in the theory (for more details see for example Ref. [5]). Some supersymmetric models also include vectorlike matter, and thus have ϕ and ψ_{VL} both present, along with many superpartners.

The phenomenology of a CP -odd scalar at the LHC can be quite distinct as compared to a CP -even scalar (such as the SM Higgs boson), and one focus of this work is to elucidate this aspect. If CP invariance is not spontaneously broken by an A vacuum expectation value (VEV), i.e. if $\langle A \rangle = 0$, as we assume here, AW^+W^- , AZZ (collectively called AVV couplings), and also $A\gamma\gamma$ and $AZ\gamma$ couplings cannot arise from renormalizable operators. The latter two also do not arise from renormalizable operators because of unbroken electromagnetic (EM) gauge invariance, the same reason why $h\gamma\gamma$ and $h\gamma Z$ are zero at the renormalizable level. These can then only result from higher-dimensional operators generated at loop level. In contrast, for the CP -even SM Higgs boson (denoted as h), the hW^+W^- and hZZ couplings are generated at tree level from dimension-four operators after electroweak symmetry breaking (EWSB), i.e. with $\langle h \rangle = v/\sqrt{2}$. Therefore, generically speaking, the AW^+W^- and AZZ effective couplings, generated at loop level, are much smaller in magnitude compared to the

^{*}shri@imsc.res.in[†]tuhin@imsc.res.in[‡]soumyasad@imsc.res.in

tree-level hW^+W^- and hZZ couplings; the $A\gamma\gamma$ and $h\gamma\gamma$ effective couplings are both loop suppressed and small, and similarly the $A\gamma Z$ and $h\gamma Z$ are also both loop suppressed. Thus, similar to the h , the $gg \rightarrow A$ “gluon-fusion” channel is important at the LHC, while compared to the h , the vector-boson fusion channel of A is much suppressed. The alternate possibility of $\langle A \rangle \neq 0$ is not discussed here but is considered for instance in Refs. [6].

Turning next to $\phi = \{A, H\}$ couplings to fermions, we include ϕ couplings to new vectorlike fermions at the tree level. Furthermore, if ϕ is part of a doublet, it couples also to SM fermions at the tree level (similar to h). We consider the case when ϕ couples significantly only to third-generation SM fermions, a situation common in many BSM extensions. Thus, the relevant couplings to SM fermions are $\phi b\bar{b}$, $\phi\tau^+\tau^-$ and $\phi t\bar{t}$. If the $\phi b\bar{b}$ coupling is sizable, $b\bar{b} \rightarrow \phi$, $bg \rightarrow b\phi$ and $gg \rightarrow b\bar{b}\phi$ can be important production channels of the ϕ . However, we do not include these production channels in this work, but restrict ourselves only to the gluon-fusion channel.

We mostly restrict ourselves to the situation when $m_\phi < 2M_{VL}$ so that ϕ cannot decay to a pair of VLFs. If the ψ_{VL} is light enough they can also be studied directly at the LHC, as discussed for instance in Ref. [5] and references therein. However, if they are too heavy to be directly produced at the LHC, but the ϕ (or h as studied in Ref. [7]) can be directly produced and its couplings measured, the VLF contributions to the ϕ effective couplings we derive here can be useful in probing the ψ_{VL} indirectly.

We identify the lighter CP -even state (h) to be the 125 GeV state discovered, and whose properties measured, at the LHC. The h couplings measured at the LHC so far largely agree with the SM, at least to about a few tens of percent, and the magnitude of the hVV coupling (with $V = \{W_\mu^\pm, Z_\mu\}$) is constrained to be close to the SM coupling at the few tens of percent level. This will be realized in the so-called “decoupling limit” [8], or more generally in the “alignment limit” [9]. In order to capture many different BSM models, we perform a model-independent effective theory analysis of the ϕ coupled to SM fields. We present the constraints from the recent 8 TeV LHC run using the $\gamma\gamma$, $\tau^+\tau^-$ and $t\bar{t}$ channels, and present the signal cross section (CS, σ) at the LHC as a function of the effective couplings of the ϕ (denoted by κ) and the branching ratio (BR) into these modes. We do not focus much on the ZZ and W^+W^- decay channels of the ϕ as the branching ratios into these modes are much smaller than the other modes due to AVV coupling being generated only at the loop level, and the HVV coupling being zero in the alignment limit. We also present many simple models containing A and ψ_{VL} in $SU(2)$ singlet and doublet representations. For A in a doublet, we restrict ourselves to the two-Higgs-doublet model (2HDM) Type II and Type X. We present the 1-loop analytical expressions for the $\{A_{gg}, A_{\gamma\gamma}, A_{\gamma Z}\}$ effective couplings induced by SMFs and

VLFs in each of these models; as a function of the model parameters, we plot numerically these effective couplings and the BR into the $\gamma\gamma$, γZ and fermion final states. These are some of the main results of this work.

In previous studies, one of us has considered the implications of models with VLQs and VLLs coupled to the lighter CP -even Higgs boson h in Ref. [7], and the direct LHC signatures of VLQs in Refs. [5]; this work provides a complement by considering aspects of heavier neutral CP -odd and CP -even scalars A, H . In Ref. [10] we study many aspects dealt with in this paper but in a specific little-Higgs model, the $SU(6)/Sp(6)$ model by Low, Skiba and Smith [11]. We also list there many little-Higgs models that contain a 2HDM structure. The results of this paper are useful in deriving constraints and prospects of such models.

From the vast literature, we give a sampling below of studies that deal with extra BSM neutral scalars, have overlap with our work, and that take into account the recent LHC 8 TeV constraints. We also mention how our work complements them. There exist several studies which present $\sigma(pp \rightarrow A)$ (see for example Refs. [12,13]) in the context of 2HDM, minimal supersymmetric standard model (MSSM) and next-to-MSSM. We highlight the effects of VLFs on $\sigma(gg \rightarrow A)$ in various SM extensions including the 2HDM-II and 2HDM-X. References [14,15] consider the possibility that the observed 125 GeV state at the LHC is a CP -odd scalar, and the former shows that this possibility is disfavored by the LHC data. References [16,17] analyze 2HDM Types I and II taking into account the 125 GeV LHC data, all pre-LHC constraints and results of the heavy-Higgs searches in various channels. Reference [18] performs a global fit of general 2HDMs using ATLAS, CMS and Tevatron results. References [19–23] shows the allowed parameter space of the 2HDM-II, applying theoretical (perturbativity, unitarity and vacuum stability) and experimental (LEP, Tevatron and LHC 125 GeV Higgs data, precision observables and B -physics and electric dipole moment measurements) constraints. Reference [24] also includes the heavy Higgs exclusion limits to constrain the 2HDM. LHC 8 TeV constraints on the 2HDM parameter space are also discussed in Refs. [25–29]. The heavy neutral scalars of the 2HDM, namely A and H , are studied in Ref. [30], where the LHC 8 TeV exclusion and 14 TeV reach from the processes $gg \rightarrow H \rightarrow AZ$ and $gg \rightarrow A \rightarrow HZ$ are presented. Reference [31] constructed an $SO(5)$ symmetric 2HDM which naturally realizes the alignment limit and puts constraints on its parameter space from the 8 TeV LHC data. Reference [32] puts limits on the triple Higgs couplings and presents a set of benchmark points for probing SM-Higgs pair production and the search of heavy Higgs bosons through nonstandard decay channels (i.e decays of A, H that involve at least one Higgs boson in the final state). Reference [33] calculates the loop factors for the AVV couplings in the MSSM and the 2HDM with a heavy chiral

fourth generation. Reference [34] studies $A \rightarrow WW$, ZZ decays and compares this with the corresponding CP -even scalar decays in the 2HDM-II, and also with a chiral fourth generation or additional heavy VLQs added. In addition to these, here we also include the effects of VLFs on $A \rightarrow \gamma\gamma$, $Z\gamma$ decays. An effective Lagrangian analysis of new heavy scalar particles is presented in Ref. [35]. Various VLF models and related phenomenological issues are also studied in Refs. [36]. Many of these studies are done with specific models in mind while we present the LHC limits and signal CS in a model-independent manner, and, using these, derive results for the models we introduce and also for some of the models above.

The paper is organized as follows: In Sec. II we present a model-independent analysis of the CP -odd and CP -even neutral scalars ϕ , present constraints on its effective couplings from the 8 TeV LHC run, the LHC gluon-fusion CS, and BR into SM fermion and gauge boson decay modes. In Sec. III we present many simple models containing ϕ and ψ_{VL} as $SU(2)$ singlets or doublets. For each of these models, we work out the 1-loop effective couplings of the ϕ and present its BR into two-body decay modes. One can read out the current constraints and gluon-fusion CS of the ϕ at the LHC for each of these models in conjunction with the results in Sec. II. The models considered include ϕ as an $SU(2)$ singlet, or as contained in the 2HDM, with correspondingly the ψ_{VL} also in singlet or doublet representations. We offer our conclusions in Sec. IV. For the various models we discuss, we compile expressions for the mass eigenvalues and mixing angles in Appendix A, and the 1-loop effective couplings in Appendix B.

II. MODEL-INDEPENDENT ANALYSIS

In this section, we define an effective Lagrangian with couplings of the neutral scalars, CP -odd A and CP -even h , H to SM gauge bosons and fermions. We denote the neutral scalars collectively as ϕ . In models that contain two CP -even scalars, we identify the lighter one (h) as the 125 GeV scalar observed at the LHC. For the heavier states (A , H), we show the constraints from the 8 TeV LHC, signal CS $\sigma \times \text{BR}$ into various SM two-body final states at the 8 and 14 TeV LHC, as a function of the effective couplings and m_ϕ . For any given new physics model, one can obtain this effective Lagrangian by integrating out heavier fields, following which the results of this section can then be used to obtain the LHC limits and gluon-fusion cross section in that model.

CP invariance requires the CP -odd scalar A coupling to SM gauge bosons to be *only* via higher-dimensional operators. The CP -even scalars can couple to the massive gauge bosons at tree level. Showing only the new physics terms, the effective Lagrangian for any neutral scalar ϕ is

$$\begin{aligned} \mathcal{L}_{\text{eff}} = & \frac{1}{2} \partial_\mu \phi \partial^\mu \phi - \frac{1}{2} m_\phi^2 \phi^2 - y_{\phi f_i f_i} \phi \bar{f}_i X f_i + y_{\phi WW} \phi W^\mu W_\mu \\ & + y_{\phi ZZ} \phi Z^\mu Z_\mu - \frac{1}{64\pi^2 M} \kappa_{\phi\gamma\gamma} \phi Y_{\mu\sigma\tau} F^{\sigma\tau} F^{\mu\nu} \\ & - \frac{1}{32\pi^2 M} \kappa_{\phi\gamma Z} \phi Y_{\mu\sigma\tau} F^{\sigma\tau} Z^{\mu\nu} - \frac{1}{64\pi^2 M} \kappa_{\phi gg} \phi Y_{\mu\sigma\tau} G^{\sigma\tau} G^{\mu\nu} \\ & - \frac{1}{64\pi^2 M} \kappa_{\phi ZZ} \phi Y_{\mu\sigma\tau} Z^{\sigma\tau} Z^{\mu\nu} \\ & - \frac{1}{32\pi^2 M} \kappa_{\phi WW} \phi Y_{\mu\sigma\tau} W^{\sigma\tau} W^{\mu\nu}, \end{aligned} \quad (1)$$

where $X = \gamma_5$, $Y_{\mu\nu\sigma\tau} = \epsilon_{\mu\nu\sigma\tau}$ for the CP -odd scalar, while $X = I$ (identity matrix), $Y_{\mu\nu\sigma\tau} = g_{\mu\sigma} g_{\nu\tau}$ for the CP -even scalar. Here $\kappa_{\phi ij}$ s contain other fermion and gauge boson loop contributions. Tree-level scalar gauge boson couplings $y_{\phi ZZ}$, $y_{\phi WW}$ are zero for the A . We have defined the dimensionless effective couplings κ by pulling out a new physics mass-scale M in the effective ϕVV terms. For the numerical results we show, we set $M = 1$ TeV from now on and show only κ ; for other values of M , the κ can easily be rescaled. Although we have defined the effective couplings κ by extracting a heavy new physics mass-scale M , SM fermion contributions are to be included when present. Equation (1) is an effective Lagrangian at a scale just above m_ϕ . Heavy BSM fermion and the SM fermion contributions are to be included in κ before comparing with the plots we show in this section. For various simple SM extensions detailed in Sec. III we compute the κ 's and present them in Appendix A. If SM fermions contribute and can go on shell, the κ are complex. In this case, the $\kappa_{\phi VV}$ that appear in our plots in this section should be read as $|\kappa_{\phi VV}|$. We assume $y_{\phi f_i f_i}$ to be real in this work.

The CP -odd scalar can decay to SM gauge bosons or fermions. In terms of the κ 's and y 's defined above, the decay rates to different final states are

$$\begin{aligned} \Gamma(\phi \rightarrow Z\gamma) &= \frac{1}{32\pi} \left(\frac{\kappa_{\phi Z\gamma}}{16\pi^2 M} \right)^2 m_\phi^3 (1 - r_Z)^3, \\ \Gamma(\phi \rightarrow gg) &= \frac{1}{8\pi} \left(\frac{\kappa_{\phi gg}}{16\pi^2 M} \right)^2 m_\phi^3, \\ \Gamma(\phi \rightarrow ff) &= \frac{N_c}{8\pi} y_{\phi ff}^2 m_\phi (1 - 4r_f)^{n/2}, \\ \Gamma(\phi \rightarrow \gamma\gamma) &= \frac{1}{64\pi} \left(\frac{\kappa_{\phi\gamma\gamma}}{16\pi^2 M} \right)^2 m_\phi^3, \end{aligned} \quad (2)$$

where $n = 3$ and $n = 1$ for CP -even and CP -odd scalars respectively, $r_f = m_f^2/m_\phi^2$, $r_Z = m_Z^2/m_\phi^2$ with $N_c = 3$ for quarks and $N_c = 1$ for leptons. Here we have defined $\Gamma(\phi \rightarrow gg)$ to have an extra factor of 8 compared to $\Gamma(\phi \rightarrow \gamma\gamma)$ anticipating a color factor. It turns out, however, that for a quark in the loop, the color factor in the $\Gamma(\phi \rightarrow gg)$ is actually 2. This will get compensated for in $\kappa_{\phi gg}$ [see for example Eq. (B1)]. Using these expressions, one can work

out the BR of the ϕ into these final states in any new physics model.

We turn next to discussing limits from the 8 TeV LHC and the gluon-fusion cross section at 14 TeV. To obtain the limits on the effective couplings κ and y , we use upper limits (ULs) from recent LHC analysis on $\sigma(pp \rightarrow \phi) \times \text{BR}(\phi \rightarrow XX)$, and the currently relevant constraints are $XX = \{\gamma\gamma, \tau^+\tau^-, t\bar{t}\}$. We take the limits on the $\gamma\gamma$ channel from the CMS analysis Ref. [37] which has an upper limit up to M_ϕ of 850 GeV, on the $\tau^+\tau^-$ channel from the ATLAS analysis Ref. [38] up to M_ϕ of 1000 GeV, and from the ATLAS analysis Ref. [39] for the $t\bar{t}$ channel. Using these we constrain the effective couplings of Eq. (1).

At the LHC, the ϕ can be produced by $gg \rightarrow \phi$ (called the gluon-fusion channel), which starts at the 1-loop level when ϕ couples to colored fermions. In addition to the above production channel, if ϕ couples to b -quarks, there are additional production channels, namely $b\bar{b} \rightarrow \phi$ (called $b\bar{b}$ -fusion), $bg \rightarrow b\phi$ and $gg \rightarrow b\bar{b}\phi$ (called b -quark associated production) channels; how these compare with the gluon-fusion channel depends on how large the $b\bar{b}\phi$ coupling is in a given model. For instance, for $y_{b\phi} = 0.5$, we find that the production rate via $b\bar{b}$ -fusion and b -quark associated production channels becomes comparable to the gluon-fusion channel with $\kappa_{\phi gg} \approx 20$. We include only the gluon-fusion channel in this study, but in models with a large $b\bar{b}\phi$ coupling, the $b\bar{b}$ -fusion and b -quark associated production channels may have to be included, which we do not do here. For a study involving the b -quark associated production channels of the h including $gg \rightarrow b\bar{b}h$, see Ref. [40]. One can separately study the b -quark associated production channels by tagging on the final state b -jet as discussed in Ref. [38]. Reference [41] has recently studied $b\bar{b}$ -fusion and b -quark associated production channels for a light CP -odd scalar. Although there are some LHC limits using b -tagged events to which the $b\bar{b}$ decay mode and the b -quark associated production channels contribute, we do not include them in our analysis here. So far these results have been presented for $m_\phi < 350$ GeV (see Refs. [42–44]).

Rather than compute the A, H production rate at the LHC ourselves, we relate it to the SM Higgs production rate at the same mass, and make use of the vast literature on the h production rate. Since $\sigma(gg \rightarrow \phi) \propto \Gamma(\phi \rightarrow gg)$, we can write the $\sigma * \text{BR}$ for ϕ production followed by decay into the final-state XX as

$$\sigma(gg \rightarrow \phi) = \frac{\Gamma(\phi \rightarrow gg)}{\Gamma(h \rightarrow gg)} \times \sigma(gg \rightarrow h). \quad (3)$$

We compute $\Gamma(\phi \rightarrow gg)$ and $\text{BR}(\phi \rightarrow XX)$ as a function of the effective couplings and apply the UL from the 8 TeV LHC quoted above using Eq. (3). For our numerical work, we take $\sigma(gg \rightarrow h)$ from Ref. [45]. We assume here that the dependence on the parton distribution function and the

acceptance at the LHC for A, H and h are not very different, which should be reasonable assumptions. For the decay $A \rightarrow XX$, the final states XX we consider are $\gamma\gamma, \tau^+\tau^-$ and $t\bar{t}$ as these are currently the significant ones. We compute the $\text{BR}(A \rightarrow XX)$ using Eq. (2). If A, H are fairly close in mass, i.e. closer than the experimental resolution to separate them (say 30% of m_ϕ), and no kinematic variables can separate them, we should include all of them into the $\sigma \times \text{BR}$ above.

In Fig. 1 we show $\sigma(gg \rightarrow \phi)$ at the 8 TeV LHC (left plot) and 14 TeV LHC (right plot) as a function of $\kappa_{\phi gg}$. $\sigma(gg \rightarrow \phi)$ is obtained using Eq. (3) and the $\sigma(gg \rightarrow h)$ from Ref. [45] as mentioned earlier. In a given new physics model, one can compute $\kappa_{\phi gg}$ and then use these plots to obtain the $\sigma(gg \rightarrow \phi)$. Using the $\sigma(gg \rightarrow \phi)$, we obtain constraints from the 8 TeV LHC data as a function of the BR into a particular mode. We show this in Fig. 2 obtained from the $\gamma\gamma, \tau^+\tau^-$ and $t\bar{t}$ channels. The regions to the top and right of the curves are excluded at the 95% C.L. level. In the $\gamma\gamma$ channel, the bound is strongest for $m_\phi = 200$ GeV since the experimental exclusion is tightest at that mass. We see that there is no constraint from this channel for $\text{BR}(\phi \rightarrow \gamma\gamma) \lesssim 10^{-4}$ for the range of $\kappa_{\phi gg}$ shown. From the $\tau^+\tau^-$ channel, we find the strongest limit for m_ϕ of about 500 GeV since the experimental exclusion is tightest at that mass. We show in Fig. 3 the total $\sigma(gg \rightarrow \phi) \times \text{BR}(\phi \rightarrow XX)$ contours (in pb) for $XX = \{\gamma\gamma, \tau^+\tau^-, t\bar{t}\}$ at the 14 TeV LHC, making use of the fact that the total $\sigma(gg \rightarrow \phi \rightarrow XX) \propto \kappa_{\phi gg}^2 \times \text{BR}(\phi \rightarrow XX)$, omitting kinematic factors independent of couplings. Thus, each mode XX can be considered and presented independently of the others as we do here. The 95% C.L. LHC exclusion discussed above is also shown labeled as “8 TeV.” If the ϕbb coupling is large, i.e. bigger than about 0.5, inclusion of the b -fusion and b -associated production channels (along with the ϕgg channel that we have included here) could result in a stronger exclusion than we obtain here.

As already mentioned, the model-independent results presented in this section can be used to obtain the LHC constraints and gluon-fusion CS in any particular model by computing first the effective couplings in that model. We next compute the effective couplings in many simple models.

III. MODELS

In this section we consider some specific models for the neutral CP -odd and CP -even scalars A, H and study their LHC production and decays into two-body final states. We compute the decay rates assuming a sharp turn-on at threshold of the two-body final state. The goal is to capture in simple models many of the features present in realistic BSM models as far as the LHC phenomenology of A, H is concerned. As before, we collectively denote A, H as ϕ . We mostly focus on the situation when $m_\phi < 2M_{VL}$ and do not focus on the phenomenology due to the ϕ decaying to a pair of on-shell VLF. We first consider the models where ϕ is an

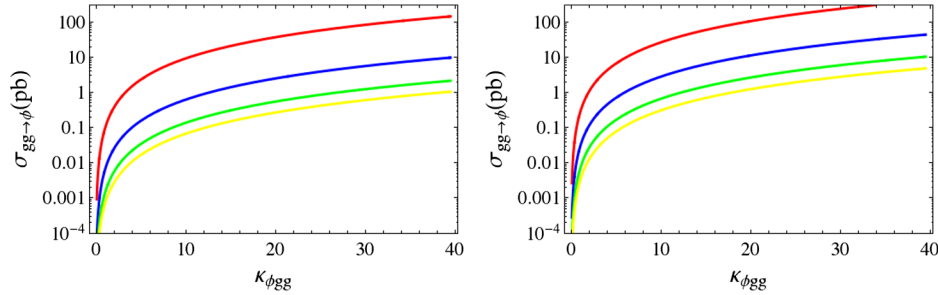


FIG. 1. $\sigma(gg \rightarrow \phi)$ (in pb) at the 8 TeV LHC (left) and 14 TeV LHC (right) for $m_\phi = 200$ GeV (red), 500 GeV (blue), 800 GeV (green) and 1000 GeV (yellow).

$SU(2)$ singlet and couples to $SU(2)$ singlet VLF [singlet A with a vectorlike up-type singlet (SVU model), or with a down-type singlet (SVD model)] and $SU(2)$ doublet VLF [singlet A with minimal vectorlike quark doublet (SVQ model)]. We next consider effective models with ϕ in an $SU(2)$ doublet, with the two $SU(2)$ doublet scalars Φ_1 and Φ_2 both having hypercharge $+1/2$. The 2HDMs we consider are either Type-II-like or Type-X-like. We notate the Type-II-like models, for example, as $MVQD$ for minimal vectorlike extension with VLQ doublet Q and down-type VLQ singlet D , and $MVQU$ for a similar model with an up-type VLQ singlet U , and a similar model with the 2HDM Type-X structure instead as $MVQDX$. We include subscripts depending on which Higgs doublets the fermions couple to, i.e. $MVQD_{ij}$ will mean that the model has one VL-quark doublet ψ , and one down-type VL-quark singlet χ , with the couplings $\bar{\psi}_L \chi_R \Phi_i$ and $\bar{\psi}_R \chi_L \Phi_j$ turned on. Among our example models are some that mimic BSM models that have ϕ Yukawa couplings with an SMQ and a VLQ, for example, the third-generation SMQ with an up-type singlet VLQ to give the MVU model.

Many of the effects we present are similar for the CP -odd and CP -even scalars A , H . One important difference between the A and H is that at tree level, the AVV (with

$V = \{W, Z\}$) couplings are zero and are only generated by SM and BSM fermions at the loop level, while the HVV couplings could be nonzero at tree level. However, in the alignment limit we consider (discussed later) the HVV couplings are zero. Thus in the alignment limit the A and H have very similar phenomenology. Therefore we will mostly present the phenomenology of the CP -odd scalar A , and, where relevant, we will also contrast it with the situation for the H . Since the tree-level HVV coupling is zero in the alignment limit, in the Appendix we only give the expressions for the fermion contributions to the $\kappa_{\phi VV}$. For the SM Higgs we must include the W loop contribution to $\kappa_{H\gamma\gamma}$ and $\kappa_{HZ\gamma}$ which we do not present here.

A. Model with an $SU(2)$ singlet A with VLQ-VLQ Yukawa couplings

We start by considering some models with an $SU(2)$ singlet A coupled to $SU(2)$ singlet or doublet VLFs. For an $SU(2)$ singlet ϕ one cannot write Yukawa couplings with chiral SMFs, and thus $gg\phi$ and $\gamma\gamma\phi$ couplings can only be induced by VLFs, if they are present, as we explicitly show here. Thus, LHC signals of a BSM singlet ϕ becomes possible if colored VLFs are coupled to it.

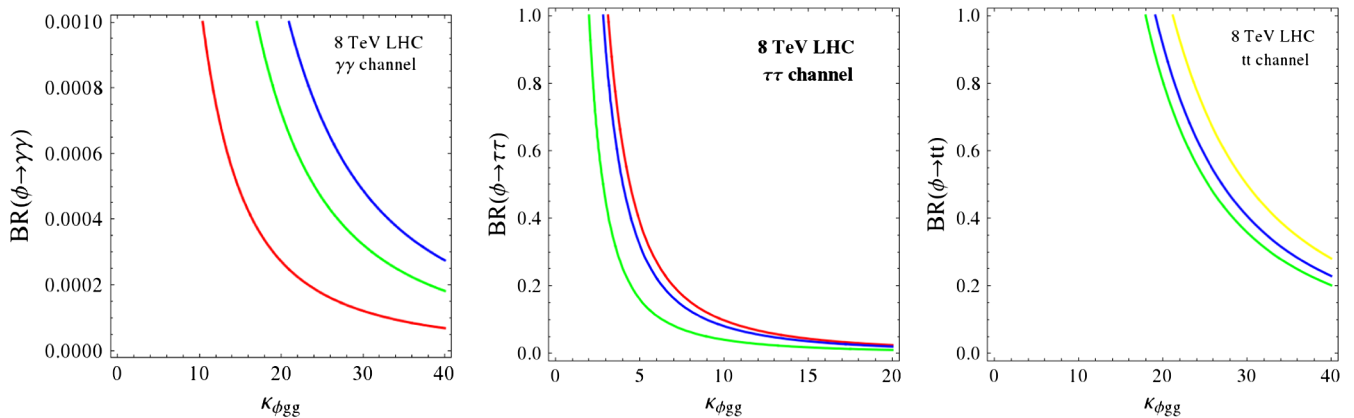


FIG. 2. 8 TeV LHC constraints from the $\gamma\gamma$ channel (left), $\tau^+\tau^-$ channel (middle) and $t\bar{t}$ channel (right), for $m_\phi = 200$ GeV (red), 500 GeV (green), 800 GeV (blue) and 1000 GeV (yellow). The regions to the top and right of the curves are excluded at the 95% C.L. level.

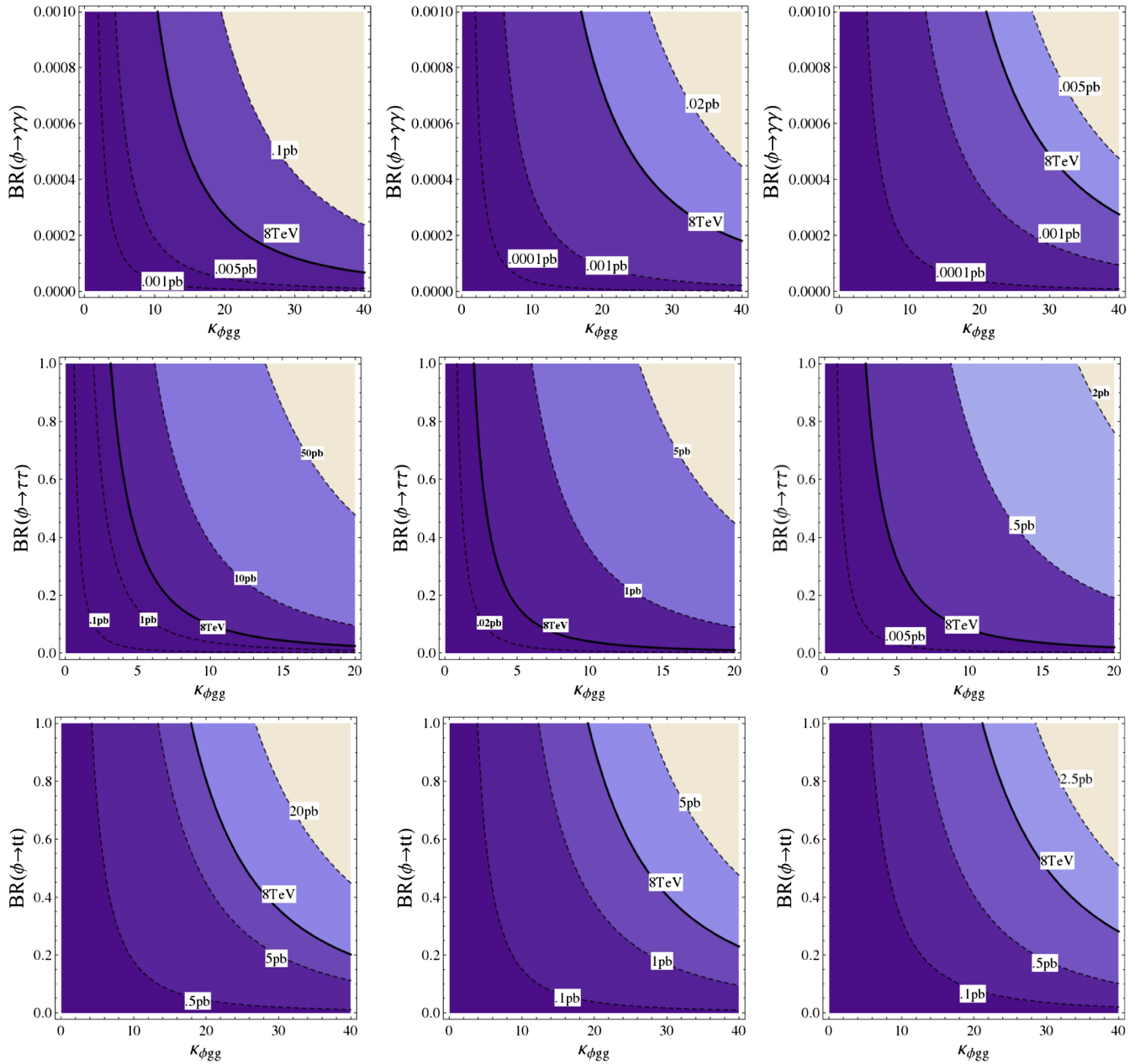


FIG. 3. Contours of the 14 TeV LHC $\sigma \times \text{BR}$ (in pb) in the $\gamma\gamma$ channel (upper row) and the $\tau^+\tau^-$ channel (middle row) for $m_\phi = 200$ GeV (left), 500 GeV (middle), 800 GeV (right), and in the $t\bar{t}$ channel (bottom row) for $m_A = 500$ GeV (left), 800 GeV (middle), 1000 GeV (right). The region to the right of the contour labeled “8 TeV” is excluded at the 95% C.L. level from 8 TeV LHC result.

1. SVU model

We study a model, which we call the *SVU* model, with an $SU(2)$ singlet CP -odd scalar A , coupled to an $SU(2)$ singlet, $SU(3)$ triplet VLQ (ψ) with hypercharge Y_ψ .¹ Clearly, the electromagnetic charge $Q = Y_\psi$. To the SM Lagrangian we add

$$\begin{aligned} \mathcal{L} \supset & \frac{1}{2} \partial_\mu A \partial^\mu A - \frac{1}{2} m_A^2 A^2 + \bar{\psi} i \not{\partial} \psi + e Q A_\mu \bar{\psi} \gamma^\mu \psi \\ & - g Q \frac{s_W^2}{c_W} Z_\mu \bar{\psi} \gamma^\mu \psi + \bar{\psi} i \not{D} \psi - i y_A A \bar{\psi} \gamma_5 \psi \\ & - m_\psi \bar{\psi} \psi - \frac{\lambda_A}{6} A^2 H^\dagger H. \end{aligned} \quad (4)$$

¹A model with only a vectorlike lepton singlet is uninteresting for A phenomenology since no LHC production channels are significant (note that the $Ab\bar{b}$ coupling is also not possible in this case).

The SM Higgs doublet is written as H here. Here we have not considered possible terms coupling the A to a SM fermion and a VLF for $Y_\psi = 2/3, -1/3$ such as $\bar{\psi}_L A u_R, \bar{\psi}_L A d_R, \bar{q} H \psi_R$. We study this possibility of off-diagonal

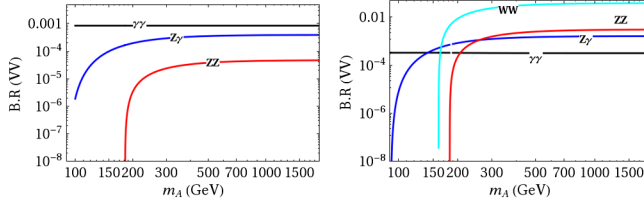


FIG. 4. $\text{BR}(A \rightarrow \gamma\gamma)$ (black), $\text{BR}(A \rightarrow \gamma Z)$ (blue), $\text{BR}(A \rightarrow ZZ)$ (red), $\text{BR}(A \rightarrow WW)$ (cyan) as a function of m_A with $y_A = 0.1$ and $m_\psi = 1000$ GeV for the *SVU* (left) and *SVQ* (right) models.

couplings between the third-generation SMQ and a VLQ in the context of the $SU(2)$ doublet Φ in Sec. III B 3.

We restrict ourselves to $m_A < 2M_{VL}$, so that A cannot decay to a VLF pair. The possible decay modes of A are to gg , $\gamma\gamma$, $Z\gamma$ and ZZ through a VLF loop, but no decay to W^+W^- . A cannot decay to a pair of SM fermions since such couplings are forbidden by gauge invariance. The effective $AV^\mu V^\nu$ couplings induced by VLFs are given in Appendix B. From these we compute the partial widths and the BR into the above modes. In Fig. 4 we plot $\text{BR}(A \rightarrow \gamma\gamma)$, $\text{BR}(A \rightarrow Z\gamma)$ and $\text{BR}(A \rightarrow ZZ)$ where we chose $Y_\psi = 2/3$ as an example. $\text{BR}(A \rightarrow gg)$ is almost constant at around 0.999.

In Fig. 5 we plot $\kappa_{A_{gg}}/y_A^2$ as a function of m_A . From this, one can read off the $\sigma(gg \rightarrow A)$ at the 8 and 14 TeV LHC from Fig. 1 in Sec. II. The peaks in Fig. 5 are due to the VLFs going on shell, although as mentioned earlier, we do not explore its consequences in this work. In this model, the gluon-fusion CS of A is induced only through loops of the heavy VLFs due to which the 8 TeV LHC exclusion limits

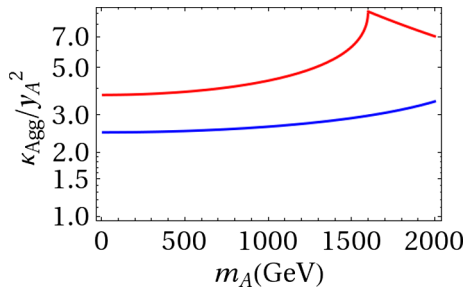


FIG. 5. $\kappa_{A_{gg}}/y_A^2$ as a function of m_A for $m_\psi = 800$ GeV (red) and 1200 GeV (blue) for the *SVU* model.

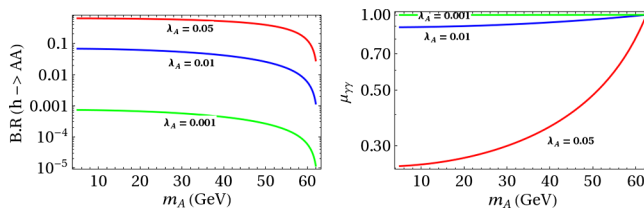


FIG. 6. $\text{BR}(h \rightarrow AA)$ (left) and $\mu_{\gamma\gamma}$ (right) as a function of m_A for the *SVU* model.

on $\sigma \times \text{BR}$ into the ZZ channel (see Ref. [46]) or the $\gamma\gamma$ channel (see Ref. [37]) are rather weak, unless y_A becomes so large that perturbativity is lost.

If $m_A < m_h/2$ (where h is the 125 GeV Higgs), then $h \rightarrow AA$ becomes kinematically allowed and becomes a means of producing A in addition to the gluon-fusion channel discussed above. In Fig. 6 we plot $\text{BR}(h \rightarrow AA)$ for $\lambda_A = 0.1, 0.05$ and 0.001 . When this decay is allowed, it will contribute to the Higgs total width thereby modifying the BRs into the other channels. In particular, it will modify the signal strength $\mu_{\gamma\gamma} = \Gamma(h \rightarrow \gamma\gamma)/\Gamma_{\text{SM}}(h \rightarrow \gamma\gamma)$, which is measured to about 10% precision (see for example Ref. [47]). We plot $\mu_{\gamma\gamma}$ in Fig. 6. We thus see that the constraint on λ_A from the 8 TeV LHC is of the order of 0.01 if $m_A < m_h/2$.

2. *SVQ* model

We consider a BSM extension, which we call the *SVQ* model, with an $SU(2)$ singlet A , and one $SU(2)$ doublet vectorlike fermion $\psi = \psi_{L,R} = (\psi_{1L,R}, \psi_{2L,R})^T$ with hypercharge Y_ψ . To the SM Lagrangian we add

$$\begin{aligned} \mathcal{L} \supset & \frac{1}{2} \partial_\mu A \partial^\mu A - \frac{1}{2} m_A^2 A^2 + \bar{\psi} i \not{D} \psi - i y_A A \bar{\psi} \gamma_5 \psi \\ & - m_\psi \bar{\psi} \psi - \frac{\lambda_1}{4!} A^4 - \frac{\lambda_A}{6} A^2 H^\dagger H, \end{aligned} \quad (5)$$

where the gauge interactions of the ψ are understood and are not explicitly shown. For $Y_\psi = 1/6$ one can add the terms $y'_u \bar{\psi}_L \tilde{H} u_R + y'_d \bar{\psi}_L H d_R + i y_{2A} A \tilde{q}_L \psi_R + \text{H.c.}$,² which we will not consider here but will address in Sec. III B 3. As in the *SVU* model, there are no decays to a pair of SM fermions, but unlike there, in this model $A \rightarrow W^+W^-$ decay is also possible through the VLF loop, in addition to gg , $\gamma\gamma$, $Z\gamma$ and ZZ modes. The expressions for the effective couplings of the A to two SM gauge bosons are given in Appendix B. We take $Y_\psi = 1/6$ as an example.

In Fig. 4 we plot the BR of A into $\gamma\gamma$, $Z\gamma$, ZZ and W^+W^- modes. As in *SVU* model, the BR into gg remains almost constant at around 0.99 for $m_A \gtrsim 300$ GeV. As the $\psi_1 \psi_2 W$ coupling (g) is greater than the $\psi_i \psi_i Z$ couplings (g/c_W)($T_3 - Qs_W^2$), the BR into WW is larger than into ZZ . Again, for the same reasons explained in the *SVU* model, the exclusion limits from the 8 TeV LHC in the $\gamma\gamma$, ZZ , WW channels are rather weak in this model also.

The $\sigma(gg \rightarrow A)$ in this model is twice of what was obtained in the *SVU* model because there are two degenerate VLFs in the loop. The VLFs are degenerate because no Yukawa terms involving the SM Higgs can be written down that can split the masses after EWSB. Since no couplings to a pair of SM fermions exist, there are no b -quark initiated production processes possible.

²We use the notation $\tilde{H} = i\sigma^2 H^*$.

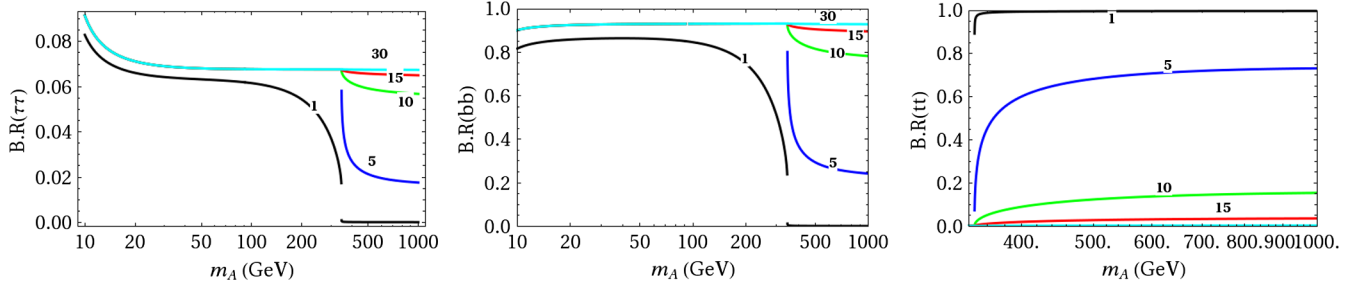


FIG. 7. $\text{BR}(A \rightarrow \tau^+ \tau^-, b\bar{b})$ (left, middle) for $\tan\beta = 1, 5, 10, 15, 30$ and $\text{BR}(A \rightarrow t\bar{t})$ (right) for $\tan\beta = 1, 5, 10, 15$ in the 2HDM Type-II model. The loop-level $\text{BR}(A \rightarrow VV)$ in the Type-II 2HDM model are shown in Fig. 16 by the dashed black curves.

B. Models with A, H in $\text{SU}(2)$ doublets (2HDM)

In the 2HDM we have two scalar doublets, Φ_1 and Φ_2 , which we take to have hypercharge $+1/2$. The physical neutral states are two CP -even scalars (h and H) and a CP -odd scalar (A). The Higgs Lagrangian is given by

$$\mathcal{L} \supset |D_\mu \Phi_1|^2 + |D_\mu \Phi_2|^2 - V(\Phi), \quad (6)$$

where

$$\begin{aligned} V(\Phi_1, \Phi_2) = & m_{11}^2 \Phi_1^\dagger \Phi_1 + m_{22}^2 \Phi_2^\dagger \Phi_2 - m_{12}^2 (\Phi_1^\dagger \Phi_2 + \text{H.c.}) \\ & + \lambda_1 (\Phi_1^\dagger \Phi_1)^2 + \lambda_2 (\Phi_2^\dagger \Phi_2)^2 + \lambda_3 (\Phi_1^\dagger \Phi_1) (\Phi_2^\dagger \Phi_2) \\ & + \lambda_4 (\Phi_1^\dagger \Phi_2) (\Phi_2^\dagger \Phi_1) + \frac{\lambda_5}{2} [(\Phi_1^\dagger \Phi_2)^2 + \text{H.c.}]. \end{aligned} \quad (7)$$

In the limit when $m_{12}^2 = 0$, the Lagrangian has a discrete Z_2 symmetry under which $\Phi_1 \rightarrow -\Phi_1$, $d_R \rightarrow -d_R$ (with all other fields unchanged), if the down-type right-handed fermions couple only to the Φ_1 and the up-type right-handed fermions only couple to the Φ_2 so that there are no tree-level flavor changing neutral currents (see for example Ref. [48]). Nonzero m_{12}^2 softly breaks this Z_2 symmetry. We will not consider the hard Z_2 breaking terms $(\Phi_1^\dagger \Phi_1 \Phi_1^\dagger \Phi_2 + \Phi_2^\dagger \Phi_2 \Phi_2^\dagger \Phi_1 + \text{H.c.})$.³ There are eight free parameters in V . After we fix the minimum of the potential at $\langle \Phi_1 \rangle = (0, v_1/\sqrt{2})^T$ and $\langle \Phi_2 \rangle = (0, v_2/\sqrt{2})^T$, with the constraint $v_1^2 + v_2^2 = v^2 = (246 \text{ GeV})^2$, the number of free parameters reduces to seven which we take to be m_A , m_h , m_H , m_{H^\pm} , $\tan\beta$, α and m_{12}^2 , in a notation that is common in the literature (see Ref. [49]). We parametrize the scalar doublets as

$$\Phi_i = \begin{pmatrix} \phi_i^+ \\ \frac{1}{\sqrt{2}}(v_i + \rho_i + i\eta_i) \end{pmatrix}, \quad (8)$$

with $v_1 = v \cos\beta$, $v_2 = v \sin\beta$ and $\tan\beta = v_2/v_1$. The physical mass eigenstates are a heavy CP -even scalar $H = \rho_1 \cos\alpha + \rho_2 \sin\alpha$, a light CP -even scalar $h = -\rho_1 \sin\alpha + \rho_2 \cos\alpha$, a CP -odd scalar $A = -\eta_1 \sin\beta + \eta_2 \cos\beta$ and charged scalars $H^\pm = -\phi_1^\pm \sin\beta + \phi_2^\pm \cos\beta$. All the effective couplings, relevant BRs and the cross sections in the 2HDM can be found in Refs. [49,50]. The expressions of α, β in terms of the model parameters can be found, for example, in Ref. [19,49]. It is these neutral scalars A, H that we are studying in this work.

In some regions of parameter space, $m_A \approx m_H$, i.e. their masses are within the experimental resolution to distinguish them. If so, we must add the contributions from both A and H to any given channel; their sum is incoherent due to the different CP quantum numbers. For instance, the experimental invariant-mass resolution in the $\tau^+ \tau^-$ channel is about 30% (see for instance Ref. [51]). Therefore, we consider two cases, one when m_A and m_H are within 30% and we add the contributions from the “degenerate” A and H , and another when they are split by more than 30% and we treat them separately. When they are degenerate, for the $\tau^+ \tau^-$ channel for instance, we have $\text{BR}(A \rightarrow \tau^+ \tau^-) \approx \text{BR}(H \rightarrow \tau^+ \tau^-)$ in the so-called alignment limit (as will be defined precisely later), and we can use the constraints obtained in Sec. II if we interpret $\kappa_{\phi gg}$ shown there as $\sqrt{\kappa_{A gg}^2 + \kappa_{H gg}^2}$ and $\text{BR}(\phi \rightarrow \tau\tau)$ as $\text{BR}(A \rightarrow \tau^+ \tau^-) + \text{BR}(H \rightarrow \tau^+ \tau^-)$. For the nondegenerate case, again one can make use of our results in Sec. II to obtain constraints either for the H or A .

We are interested in the case where the lighter CP -even scalar (h) is the observed 125 GeV Higgs boson. For this, the $\cos(\beta - \alpha) \approx 0$ is the most favored region (see Fig. 18 of Ref. [17]). Only a small range of other values of $(\beta - \alpha)$ are allowed where the sign of the down-type coupling of the Higgs is reversed. For the 2HDM with exact Z_2 symmetry (i.e. $m_{12}^2 = 0$), $\tan\beta$ has an upper limit of 7 from the perturbativity constraint (see Ref. [24]). We will work with

³This is a natural choice since if these terms are zero to start with they will not be induced at the loop level even if the soft breaking terms are present.

a nonzero m_{12}^2 which allows for larger values of $\tan\beta$ (see Ref. [20]). We also assume that the alignment limit ($\beta - \alpha = \pi/2$) holds sufficiently accurately so that the h couplings are SM-like to match with the properties of the observed 125 GeV state at the LHC as discussed in Ref. [16]. In this limit, the $H \rightarrow WW$ and $H \rightarrow ZZ$ decays do not give any significant constraints on the parameter space (see for example Ref. [46]).

Depending on how the fermions couple to Φ_1 and Φ_2 , various types of 2HDM have been defined in the literature, some of which we discuss next. We start by discussing a 2HDM with only the SM fermions present, and follow it up with many examples of different ways of adding vectorlike fermions.

1. Type-II 2HDM

In the Type-II 2HDM the SM Yukawa couplings are replaced by

$$\mathcal{L} \supset -y_d \bar{q}_L \Phi_1 d_R - y_u \bar{q}_L \tilde{\Phi}_2 u_R + \text{H.c.}, \quad (9)$$

where $\tilde{\Phi}_i = i\sigma^2 \Phi_i^*$. The Yukawa couplings of h, A to the SM fermions are given as

$$\begin{aligned} \mathcal{L} \supset & -\frac{1}{\sqrt{2}} (y_u h c_\alpha \bar{u}_L u_R - y_d h s_\alpha \bar{d}_L d_R - y_u c_\beta i A \bar{u}_L u_R \\ & - y_d s_\beta i A \bar{d}_L d_R + \text{H.c.}). \end{aligned} \quad (10)$$

The H -Yukawa couplings can be obtained from the h -Yukawa couplings by the replacements $s_\alpha \rightarrow -c_\alpha$ and $c_\alpha \rightarrow s_\alpha$. We find the allowed regions of parameter space from the exclusion limit on $\sigma(gg \rightarrow \phi) \times \text{BR}(\phi \rightarrow \tau^+ \tau^-)$ presented by ATLAS [38,51]. We focus on the $\tau^+ \tau^-$ channel as currently this is the most constraining one. We do this first in the 2HDM Type-II (2HDM-II) without the addition of any VLFs.

In Fig. 7 we show the tree-level decays of A to SM fermions $\text{BR}(A \rightarrow b\bar{b}, \tau^+ \tau^-, t\bar{t})$ as a function of m_A for various $\tan\beta$ for the Type-II 2HDM. The loop-level $\text{BR}(A \rightarrow \gamma\gamma, Z\gamma)$ in the Type-II 2HDM are shown in Fig. 16 by the dashed black curves, and our results match with those of the Ref. [50]. We see that the BRs into $\gamma\gamma$ and $Z\gamma$ are smaller compared to those of the corresponding loop-induced SM Higgs branching ratios even for $\tan\beta = 1$ when the couplings of A to the SM fermions are equal to the Higgs Yukawa couplings. This is because the partial width $\Gamma(h \rightarrow \gamma\gamma, \gamma Z)$, being dominated by the W loop, is larger than the partial width $\Gamma(A \rightarrow \gamma\gamma, \gamma Z)$ in which only the fermions contribute (see for example Fig. 2.10 of Ref. [50]). For larger $\tan\beta$ the branching ratios are even smaller because of the increased $\Gamma(A \rightarrow b\bar{b})$ and $\Gamma(A \rightarrow \tau^+ \tau^-)$ (recall that the $A b\bar{b}$ and $A \tau^+ \tau^-$ couplings are proportional to $\tan\beta$). The discontinuity at $m_A = 2m_t$ in the BRs in Fig. 16 for $\tan\beta = 1$ is because of the onset of

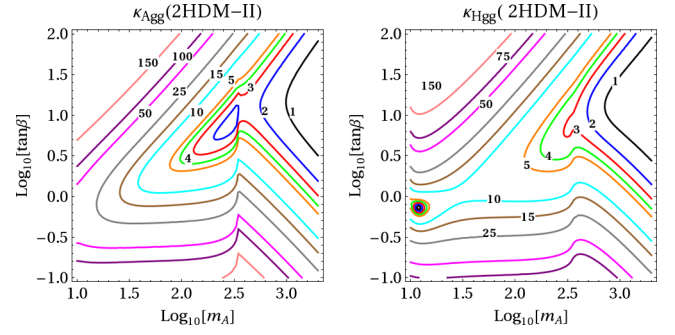


FIG. 8. Contours of $\kappa_{A_{gg}}$ (left) and $\kappa_{H_{gg}}$ (right) in the Type-II 2HDM.

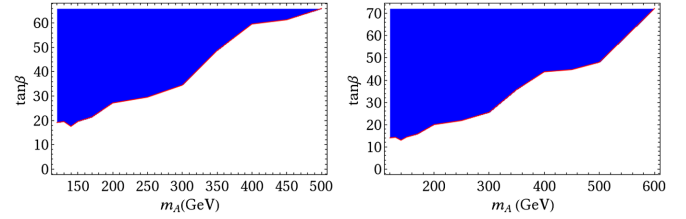


FIG. 9. For the Type-II 2HDM, regions of the m_A - $\tan\beta$ parameter space (blue region) which are excluded at the 95% confidence level from $\phi \rightarrow \tau^+ \tau^-$ decay when only A is present (left) and when m_A and m_H are degenerate (right).

$A \rightarrow t\bar{t}$ on-shell decay. For larger $\tan\beta$, the discontinuity is smaller since the $A t\bar{t}$ coupling becomes smaller. The $h \rightarrow AA$ decay, possible for $m_A < m_h/2$, is studied in Ref. [17] and we will not discuss it here.

In Fig. 8, we plot contours of $\kappa_{A_{gg}}$ and $\kappa_{H_{gg}}$ in the Type-II 2HDM. Using this, one can read off the $\sigma(gg \rightarrow \phi)$ at the 8 and 14 TeV LHC from Fig. 1 in Sec. II. Using the $\tau^+ \tau^-$ channel constraints shown in Fig. 2 of Sec. II we obtain constraints on this model. In Fig. 9 we plot the 95% confidence level constraints on the m_A - $\tan\beta$ plane, when only A is present (left), and for $m_A = m_H$ when both contribute (right). Reference [51] has presented similar constraints in the m_A - $\tan\beta$ plane, but for the MSSM.

2. Type-X 2HDM

In the Type-X 2HDM (2HDM-X) (see Refs. [28,49] for a description of this model) all the SM quarks couple to Φ_2 and all the leptons couple to Φ_1 . The Lagrangian for the model 2HDM-X is given by

$$\begin{aligned} \mathcal{L} \supset & -(y_d \bar{q}_L \Phi_2 d_R + y_u \bar{q}_L \tilde{\Phi}_2 u_R + y_e \bar{l}_L \Phi_1 e_R + \text{H.c.}) \\ & + |D_\mu \Phi_1|^2 + |D_\mu \Phi_2|^2 - V(\Phi). \end{aligned} \quad (11)$$

As a result, A coupling to the quarks and leptons are proportional to $\cot\beta$ and $\tan\beta$ respectively. In the Type-X model, since all SM quarks couple very weakly to A for large $\tan\beta$, $\sigma(gg \rightarrow A)$ becomes very small for large $\tan\beta$. As a consequence there are no constraints from

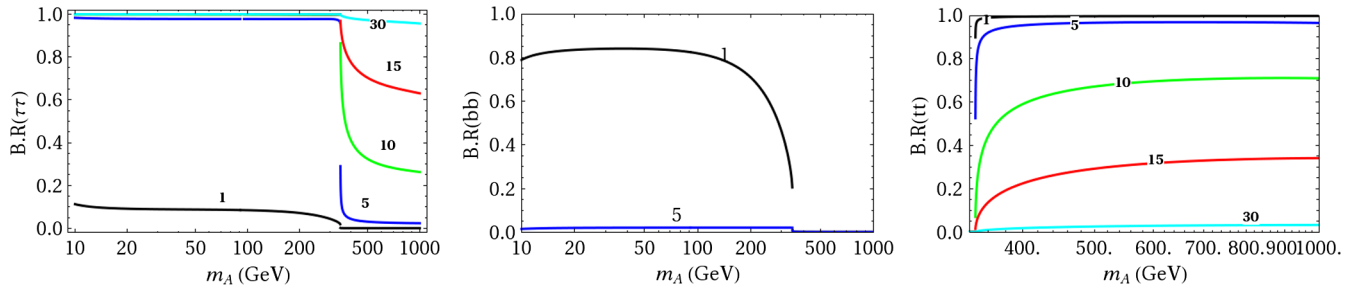


FIG. 10. For the Type-X 2HDM, $\text{BR}(A \rightarrow \tau^+\tau^-, t\bar{t})$ (left, right) for $\tan\beta = 1, 5, 10, 15, 30$, and $\text{BR}(A \rightarrow b\bar{b})$ (middle) for $\tan\beta = 1, 5$. The $\text{BR}(A \rightarrow \gamma\gamma, Z\gamma)$ for the Type-X 2HDM is shown in Fig. 27 as the dashed black curve.

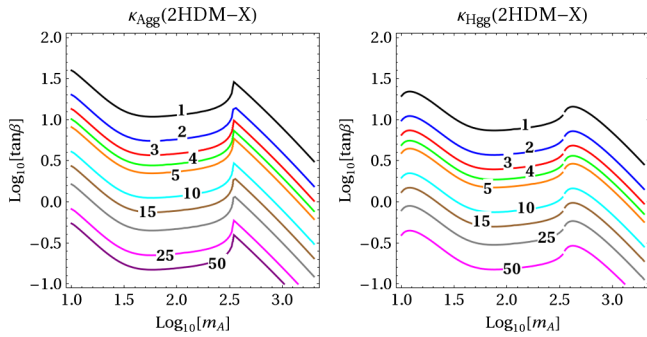


FIG. 11. For the Type-X 2HDM, contours of $\kappa_{A_{gg}}$ (left) and $\kappa_{H_{gg}}$ (right).

$\sigma(pp \rightarrow A) \times \text{BR}(A \rightarrow \tau^+\tau^-)$. The SM quark contribution to κ_{AVV} for the 2HDM-X can be obtained from that of the 2HDM-II (see Ref. [50]) by replacing $\tan\beta$ with $\cot\beta$ in the $Ab\bar{b}$ coupling. In Fig. 10 we show the tree-level $\text{BR}(A \rightarrow \tau^+\tau^-, b\bar{b}, t\bar{t})$. The $\text{BR}(A \rightarrow VV)$ for the Type-X 2HDM is shown in Fig. 27 as the dashed black curve.

In Fig. 11 we plot contours of $\kappa_{A_{gg}}$ and $\kappa_{H_{gg}}$. From this one can read off $\sigma(gg \rightarrow \phi)$ for 8 TeV and 14 TeV LHC from Fig. 1 in Sec. II. The results for $\kappa_{\phi gg}$ in the 2HDM-X are also applicable for the Type-I 2HDM as the SM quarks couple to H, A in an identical fashion as in the Type-X 2HDM.

Next, we add various combinations of $SU(2)$ singlet and doublet VLFs to the Type-II 2HDM first, and to the Type-X 2HDM following that. Our goal is to study how VLFs affect the LHC production rate and decay BRs of the ϕ . There are eight different ways in which the Φ_1 and the Φ_2 can couple to the VLFs consistent with the symmetries of the 2HDM-II, namely $\Phi_1 \rightarrow -\Phi_1$ and $d_R \rightarrow -d_R$ (with all other fields unchanged). Among these eight models we will discuss only three representative ones that also capture the effects in the others.

3. Type-II 2HDM with VLQ-SMQ Yukawa couplings

Many models that address the hierarchy problem, such as for example the composite-Higgs and the little-Higgs models, have as an important ingredient off-diagonal

couplings between a VLF and third-generation SM fermions. We discuss this possibility in a model-independent way by introducing, one at a time, $SU(2)$ -singlet VLFs with EM charge $2/3$ and $-1/3$. As an example, we show how the results obtained here apply to a little-Higgs model.

MVU model.—In what we call the *MVU* model, we introduce an $SU(2)$ -singlet VLF pair (ψ, ψ^c) , denoted by the 4-spinor ψ , with EM charge $2/3$, and add to the 2HDM Type-II Lagrangian the following terms:

$$\mathcal{L} \supset M_\psi \bar{\psi}\psi - (y_1 \bar{q}_L \tilde{\Phi}_1 \psi_R + \text{H.c.}). \quad (12)$$

After EWSB the mass terms for the EM charge $2/3$ fermions can be written as

$$\mathcal{L}^{\text{mass}} = -\frac{1}{\sqrt{2}}(y_u v_2 \bar{t}_L t_R + y_1 v_1 \bar{t}_L \psi_R + \text{H.c.}) + M_\psi \bar{\psi}\psi. \quad (13)$$

We define the mass eigenstates $t_{L,R}^0$ and $t_{2L,R}$, for the EM charge- $2/3$ quarks as

$$\begin{aligned} t_{L,R} &= \cos\theta_{L,R}^U t_{L,R}^0 - \sin\theta_{L,R}^U t_{2L,R}, \\ \psi_{L,R} &= \sin\theta_{L,R}^U t_{L,R}^0 + \cos\theta_{L,R}^U t_{2L,R}. \end{aligned} \quad (14)$$

The mixing angles and the mass eigenvalues can be found in Appendix A 1. For notational brevity we call t^0 simply as t , which we will identify with the SM top quark. Constraints on the mixing from electroweak precision tests and a vectorlike top decaying to Wb, Zt, Ht are studied in Refs. [5,7,52,53]. Constraints from flavor observables are studied in Ref. [52].

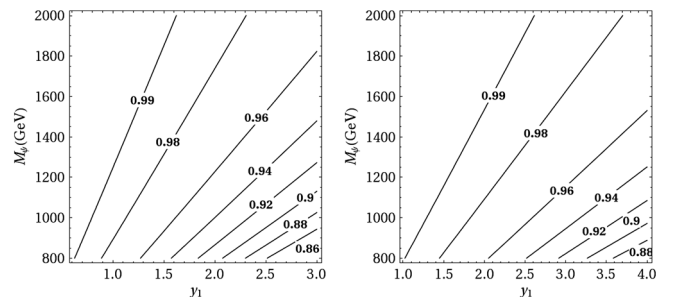


FIG. 12. For the *MVU* model, contours of $\kappa_{H_{tt}}$ for $\tan\beta = 1$ (left) and $\tan\beta = 5$ (right) with y_u chosen such that $m_t = 163$ GeV.

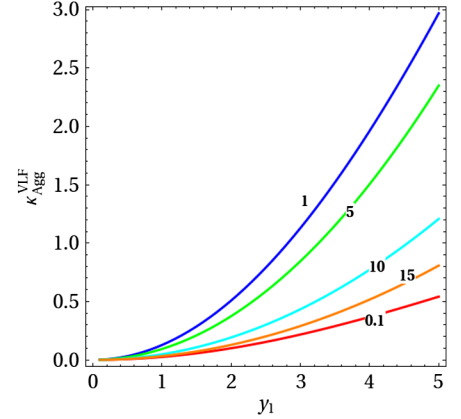
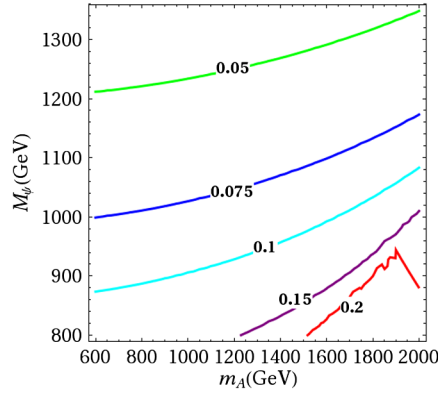
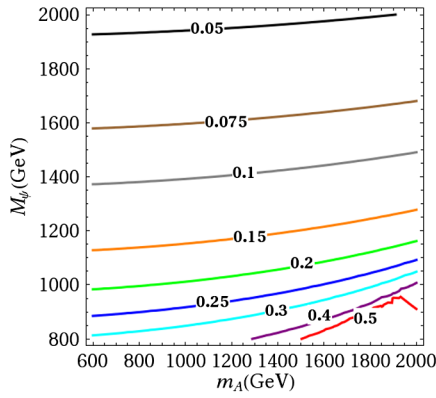


FIG. 13. Contours of $\kappa_{A_{gg}}^{\text{VLF}}/y_1^2$ for $\{\tan\beta, y_u\} = \{1, 1.4\}$ (left) and $\{5, 1\}$ (middle) for the *MVU* model. $\kappa_{A_{gg}}^{\text{VLF}}$ as a function of y_1 , for $m_A = 1000$ GeV, $M_\psi = 1250$ GeV and $\tan\beta = 0.1, 1, 5, 10, 15$ is plotted on the right.

The A couplings to the EM charge-2/3 fermions in terms of the mass eigenstates are given by

$$\mathcal{L} = \frac{i}{\sqrt{2}} A (y_{A t_1} \bar{t}_L t_R + y_{A t_2} \bar{t}_2 t_R) + \text{H.c.}, \quad (15)$$

where $y_{A t_1} \supset (y_u c_L^U c_R^U \cos\beta - y_1 c_L^U s_R^U \sin\beta)$, $y_{A t_2} = (y_u s_L^U s_R^U \cos\beta + y_1 s_L^U c_R^U \sin\beta)$, $y_{A t_2} = -(y_u s_L^U c_R^U \cos\beta - y_1 c_L^U s_R^U \sin\beta)$, and $y_{A t_2} = -(y_u c_L^U s_R^U \cos\beta + y_1 c_L^U c_R^U \sin\beta)$. The h couplings to the EM charge-2/3 fermions are given by

$$\mathcal{L} \supset \frac{1}{\sqrt{2}} h (y_{h t_1} \bar{t}_L t_R + y_{h t_2} \bar{t}_2 t_R + y_{h t_2} \bar{t}_2 t_R + y_{h t_2} \bar{t}_2 t_R) + \text{H.c.}, \quad (16)$$

where $y_{h t_1} = (-y_u c_L^U c_R^U \cos\alpha + y_1 c_L^U s_R^U \sin\alpha)$, $y_{h t_2} = (-y_u s_L^U s_R^U \cos\alpha - y_1 s_L^U c_R^U \sin\alpha)$, $y_{h t_2} = (y_u s_L^U c_R^U \cos\alpha - y_1 c_L^U s_R^U \sin\alpha)$, and $y_{h t_2} = (y_u c_L^U s_R^U \cos\alpha + y_1 c_L^U c_R^U \sin\alpha)$. We fix $m_t^{\text{MS}} = 163$ GeV [54] by choosing y_u appropriately, and show in Fig. 12 the contours of $\kappa_{h t_1} \equiv y_{h t_1}/y_{h t_1}^{\text{SM}}$ in the y_1 - M_ψ plane. In the region to the left of the 0.99 contours, $\kappa_{h t_1}$ approaches 1. The experimental constraint on $\kappa_{h t_1}$ is $0.63 < \kappa_{h t_1} < 1.2$ [55]. In Fig. 13 we show contours of $\kappa_{A_{gg}}^{\text{VLF}}/y_1^2$ in the m_A - M_ψ plane for $\{\tan\beta, y_u\} = \{1, 1.4\}$ and $\{5, 1\}$, and also show $\kappa_{A_{gg}}^{\text{VLF}}$ as a function of y_1 for $m_A = 1000$ GeV, $M_\psi = 1250$ GeV and $\tan\beta = 0.1, 1, 5, 10, 15$. For large $\tan\beta$, the mixing angles become small, which makes $\kappa_{A_{gg}}^{\text{VLF}}$ small. For Fig. 13, we fix $y_u = 1.4$ so that m_t is close to its experimental value, and once a specific choice of y_1 is made, m_t can be fixed exactly by choosing y_u slightly differently; the resulting change in $\kappa_{A_{gg}}^{\text{VLF}}$ due to such differences in y_u is insignificant.

The fermionic decay BR for $m_A < (M_{t_2} + m_t)$ will be largely unchanged from the Type-II 2HDM plots shown in Fig. 7. However, if $m_A > (M_{t_2} + m_t)$ the $A \rightarrow t_2 t$ decay

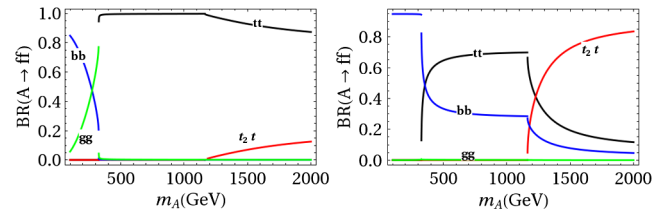


FIG. 14. Contours of $\text{BR}(A \rightarrow tt)$ (black), $\text{BR}(A \rightarrow bb)$ (blue), $\text{BR}(A \rightarrow gg)$ (green) with $M_\psi = 1000$ GeV, $y_1 = 1$ for $\tan\beta = 1$ (left) and 5 (right), for the *MVU* model, with y_u chosen such that $m_t = 163$ GeV.

becomes kinematically allowed. In Fig. 14 we plot $\text{BR}(A \rightarrow tt)$, $\text{BR}(A \rightarrow bb)$, $\text{BR}(A \rightarrow gg)$ and $\text{BR}(A \rightarrow t_2 t)$, for $M_\psi = 1$ TeV, $y_1 = 1$ and $\tan\beta = \{1, 5\}$ with y_u fixed such that m_t is at the physical value. $\text{BR}(A \rightarrow \gamma\gamma, Z\gamma)$ do not change by much from the 2HDM-II case.

As an example, we apply these results to a concrete model that stabilizes the electroweak scale, has a 2HDM structure, and has vectorlike fermions, namely the $\text{SU}(6)/\text{Sp}(6)$ little-Higgs model by Low, Skiba and Smith (LSS) [11], which we analyze in detail in Ref. [10]. Among the various sample points that are listed in Appendix B in Ref. [10] that satisfy all constraints including the precision electroweak constraints, we consider here the sample points 1 and 2. For the sample point 1, the two lightest VLFs are the t_2 with a mass of 1218 GeV, the b_2 with a mass of 1315 GeV, and we have $\tan\beta = 1.36$, $m_A = 1671$ GeV, $y_1 = 1.7$, $y_u = 1.2$ and $m_t \approx 164$ GeV.⁴ Keeping only the lighter t_2 since the t_3 is

⁴From Ref. [10] we list below a few details for the LSS model. There, we had $\tan\beta = v_1/v_2$ while in this paper we have $\tan\beta = v_2/v_1$; therefore $\tan\beta$ here is related to that of Ref. [10] via $\tan\beta = (1/\tan\beta^{\text{LSS}})$. y_1 is given by $y_1 = y_1^{\text{LSS}} c_{23}$; for point 1, since $y_1 \gg y_4$, to a very good approximation $s_{14} \approx 1$ and $c_{14} \approx 0$. Also, $m_t \approx c_{23} y_2 v_2 / \sqrt{2}$ in the limit where t_3 is decoupled away, i.e. $y_u = y_2 c_{23}$, and $c_{23} \approx 0.9$. The b_2 is an $\text{SU}(2)$ singlet since it does not mix with the other states of charge $-1/3$.

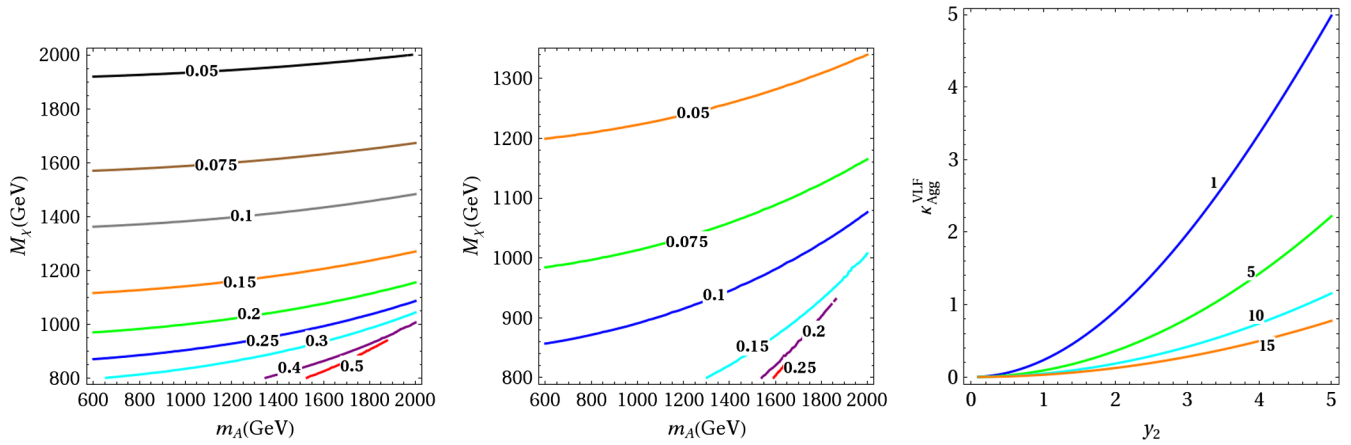


FIG. 15. Contours of k_{Agg}^{VLF}/y_2^2 for $\{\tan\beta, y_d\} = \{1, 0.03\}$ (left) and $\{5, 0.12\}$ (middle) for the *MVD* model. k_{Agg}^{VLF} with y_2 for $m_A = 1500$ GeV, $M_\chi = 1000$ GeV and $\tan\beta = 1, 5, 10, 15$ is plotted on the right.

somewhat heavier, a good approximation is obtained by considering the addition of only a singlet EM charge $+2/3$ state ψ as introduced in Eq. (12). Ignoring the smaller b_2 contribution, the κ_{Agg}^{VLF} due to the t_2 can be read off from the $\tan\beta = 1$ curve of the rightmost panel of Fig. 13 to be approximately 0.4. This is about 10% of the SM-fermion contribution.

MVD model.—In the *MVD* model, we introduce an SU(2)-singlet VLF pair (χ, χ^c) , denoted by the 4-spinor χ , with EM charge $-1/3$, and add to the 2HDM Type-II Lagrangian the following terms:

$$\mathcal{L}_A = M_\chi \bar{\chi} \chi - (y_2 \bar{q}_L \Phi_1 \chi_R + \text{H.c.}). \quad (17)$$

The mass eigenstates, $b_{L,R}^0$ and $b_{2L,R}$ for the fermions of EM charge $-1/3$ are defined in the same way as in Eq. (14) with the mixing angles $\theta_{L,R}^p$. The mixing angles and the mass eigenvalues can be found in Appendix A 1. The A couplings to the fermions of EM charge $-1/3$ are obtained in a similar way as in Eq. (15), with the replacements $y_u \cos\beta \rightarrow y_d \sin\beta$, $y_1 \rightarrow y_2$. Similarly, the h couplings to the fermions of EM charge $-1/3$ are obtained from Eq. (16), with the replacements $y_u \cos\alpha \rightarrow -y_d \sin\alpha$ and $y_1 \rightarrow y_2$. As in the case of charge- $2/3$ fermions, we choose y_d such that $m_b^{\text{MS}} = 4.2$ GeV [56]; y_{hbb} stays close to its SM value. In Fig. 15 we plot contours of κ_{Agg}^{VLF}/y_2^2 in the $m_A - M_\chi$ plane for $\{\tan\beta, y_d\} = \{1, 0.03\}$, and $\{5, 0.12\}$ and κ_{Agg}^{VLF} as a function of y_2 for $m_A = 1500$ GeV, $M_\chi = 1000$ GeV for $\tan\beta = 1, 5, 10, 15$.

As an example we consider again the LSS model, but now the sample point 2 in Appendix B of Ref. [10], with the lightest VLF being the b_2 with a mass of 947.5 GeV. The b_2 is an SU(2) singlet state and does not mix with the other states of charge $-1/3$. For this point, $m_A = 1671$ GeV, $\tan\beta = 1.36$, $y_2 = 1.422$, $c_{23} = 1.15$. κ_{Agg} can be read off from the $\tan\beta = 1$ curve of the rightmost panel of Fig. 15 to be approximately 0.3.

MVQ model.—For the *MVQ* model, we add an SU(2) doublet VLF pair (Q', Q'^c) denoted by the 4-spinor Q' , and add to the Type-II 2HDM Lagrangian the terms

$$\mathcal{L} \supset M_{QQ} \bar{Q}' Q' + (M_{qQ} \bar{q}_L Q'_R - \tilde{y}_1 \bar{Q}'_L \tilde{\Phi}_2 t_R - \tilde{y}_2 \bar{Q}'_L \Phi_1 b_R + \text{H.c.}). \quad (18)$$

In the following we show only the top sector since this is usually the dominant piece in BSM models, and we therefore suppress the bottom sector. At the outset, we diagonalize the VLF masses by redefining the Q and Q' fields by an orthogonal rotation to get an equivalent Lagrangian given by

$$\mathcal{L} \supset M_{QQ}^{\text{eff}} \bar{Q}' Q' + (-y_u^{\text{eff}} \bar{q}_L \tilde{\Phi}_2 t_R - \tilde{y}_1^{\text{eff}} \bar{Q}'_L \tilde{\Phi}_2 t_R + \text{H.c.}), \quad (19)$$

where we show the 2HDM top Yukawa coupling also since its effective coupling is now changed, with $M_{QQ}^{\text{eff}} \equiv \sqrt{(M_{QQ}^2 + M_{qQ}^2)}$, $y_u^{\text{eff}} \equiv (y_u M_{QQ} - \tilde{y}_1 M_{qQ})/M_{QQ}^{\text{eff}}$, $\tilde{y}_1^{\text{eff}} \equiv (y_u M_{qQ} + \tilde{y}_1 M_{QQ})/M_{QQ}^{\text{eff}}$, which imply $y_u^{\text{eff}} = (y_u - \tilde{y}_1 M_{qQ}/M_{QQ})/\sqrt{1 + (M_{qQ}/M_{QQ})^2}$ and $\tilde{y}_1^{\text{eff}} = y_u^{\text{eff}} M_{qQ}/M_{QQ} + \tilde{y}_1 \sqrt{1 + (M_{qQ}/M_{QQ})^2}$.

The $\kappa_{\phi gg}$ due to the t' , b' in the *MVQ* model are qualitatively similar to the *MVU* case presented earlier. As an example, let us consider again the LSS model sample point 1 in Appendix B of Ref. [10], for which we have $\tilde{y}_1 = 0$, $y_u^{\text{eff}} \approx 1.3$ and $\tilde{y}_1^{\text{eff}} \approx 0.5$, which gives $\kappa_{Agg} \approx 0.03$. The doublet-VLQ contribution in this case is thus very small compared to the SMQ contribution.

4. Type-II 2HDM with VLQ-VLQ Yukawa couplings

Here, we add SU(2) doublet and singlet VLFs with SM-like hypercharge assignments, and write Yukawa couplings

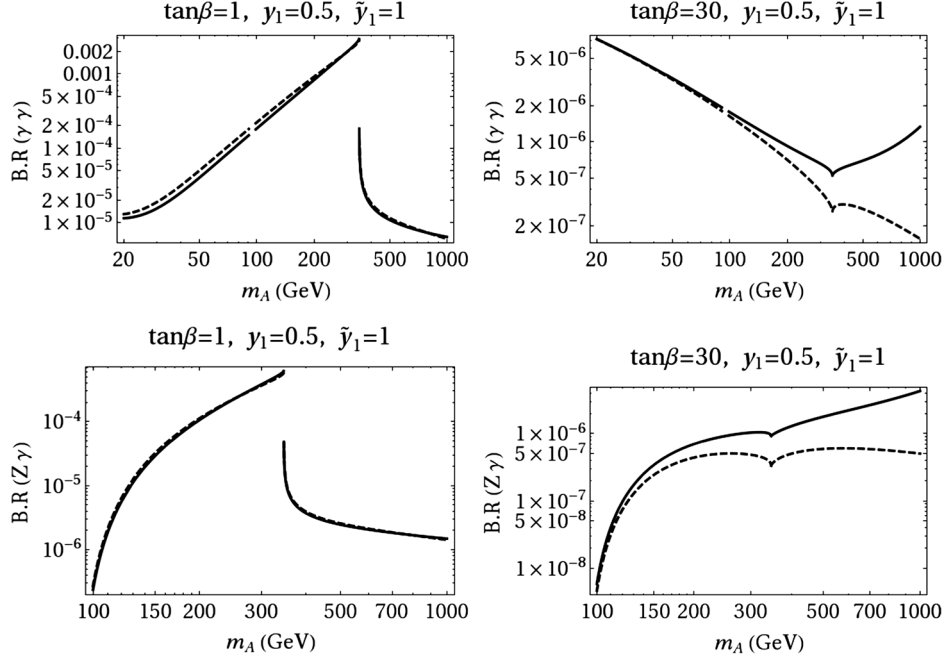


FIG. 16. BR($A \rightarrow \gamma\gamma$) (top panel) and BR($A \rightarrow Z\gamma$) (bottom panel) with $M_\psi = M_\chi = 1000$ (GeV), $\tan\beta = 1$ (left) and 30 (right) in the $MVQD_{11}$ model (solid black) and in the 2HDM Type-II (dashed black). BR($A \rightarrow f\bar{f}$) in the Type-II 2HDM are as shown in Fig. 7.

between them both involving the $\Phi_{1,2}$. Although there could be Yukawa couplings between a VLF and a SMF also present, we do not write them here for simplicity; their effects are investigated separately in Sec. III B 3.

MVQD₁₁ model.—To the Type-II 2HDM we introduce one doublet VLQ, $\psi = (\psi_1, \psi_2)$, with hypercharge Y_ψ and one singlet VLQ (χ) with hypercharge ($Y_\psi - 1/2$) so that VLF couplings with Φ_1 are allowed. The additional Lagrangian terms to the 2HDM-II are

$$\mathcal{L} \supset \bar{\psi}_i \not{D} \psi + \bar{\chi} i \not{D} \chi - (y_1 \bar{\psi}_L \Phi_1 \chi_R + \tilde{y}_1 \bar{\psi}_R \Phi_1 \chi_L + \text{H.c.}) - M_\psi \bar{\psi} \psi - M_\chi \bar{\chi} \chi. \quad (20)$$

We can also write the terms $\bar{\psi}_L \Phi_2 \chi_R$ and $\bar{\psi}_R \Phi_2 \chi_L$, which we do not add here but will consider them subsequently as another model. These terms are forbidden if $\chi \rightarrow -\chi$ under the Z_2 symmetry of 2HDM-II. The terms involving h , A and VLFs after EWSB are

$$\begin{aligned} \mathcal{L} \supset & -M_\psi \bar{\psi} \psi - M_\chi \bar{\chi} \chi + \frac{1}{\sqrt{2}} A \sin \beta (i y_1 \bar{\psi}_{2L} \chi_R + i \tilde{y}_1 \bar{\psi}_{2R} \chi_L \\ & + \text{H.c.}) - \frac{v}{\sqrt{2}} \cos \beta (y_1 \bar{\psi}_{2L} \chi_R + \tilde{y}_1 \bar{\psi}_{2R} \chi_L + \text{H.c.}) \\ & + \frac{1}{\sqrt{2}} h \sin \alpha (y_1 \bar{\psi}_{2L} \chi_R + \tilde{y}_1 \bar{\psi}_{2R} \chi_L + \text{H.c.}) \\ & - \frac{1}{\sqrt{2}} H \cos \alpha (y_1 \bar{\psi}_{2L} \chi_R + \tilde{y}_1 \bar{\psi}_{2R} \chi_L + \text{H.c.}). \end{aligned} \quad (21)$$

Gauge interactions of the VLFs are present and not shown explicitly. ψ_2 and χ mix after EWSB, while ψ_1 is

itself a mass eigenstate. We define the mass eigenstates ζ_1 and ζ_2 as

$$\psi_{2L,R} = \zeta_{1L,R} \cos \theta_{L,R} - \zeta_{2L,R} \sin \theta_{L,R}, \quad (22)$$

$$\chi_{L,R} = \zeta_{1L,R} \sin \theta_{L,R} + \zeta_{2L,R} \cos \theta_{L,R}, \quad (23)$$

where the mixing angles θ_L and θ_R are defined in Appendix A 2. In terms of these mass eigenstates, the Lagrangian in Eq. (21) can be written as

$$\begin{aligned} \mathcal{L} \supset & -y_{ij}^A (i A \bar{\zeta}_{iL} \zeta_{jR} + \text{H.c.}) - M_i \bar{\zeta}_i \zeta_i - M_\psi \bar{\psi}_1 \psi_1 \\ & + \kappa_{ij} Z_\mu \bar{\zeta}_i \gamma_\mu \zeta_j + e Q_i A_\mu \bar{\zeta}_i \gamma_\mu \zeta_i \\ & - y_{ij}^h (h \bar{\zeta}_{iL} \zeta_{jR} + \text{H.c.}) - y_{ij}^H (H \bar{\zeta}_{iL} \zeta_{jR} + \text{H.c.}), \end{aligned} \quad (24)$$

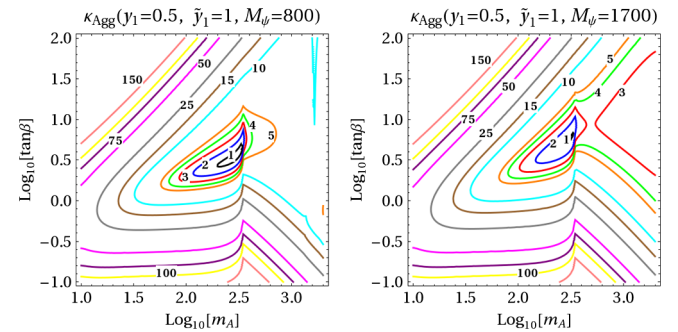


FIG. 17. Contours of κ_{Agg} for $M_\psi = M_\chi = 800$ GeV (left), 1700 GeV (right), $y_1 = 0.5$, $\tilde{y}_1 = 1$ for the $MVQD_{11}$ model.

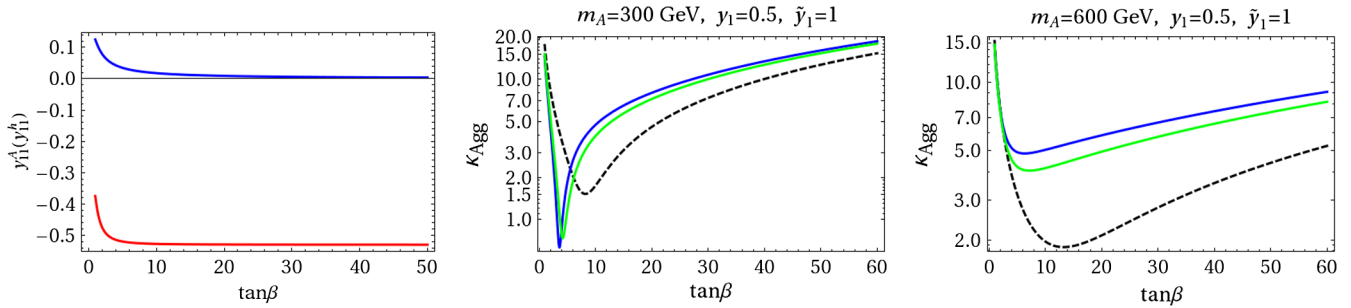


FIG. 18. For the $MVQD_{11}$ model, y_{11}^A (red), y_{11}^h (blue) as a function of $\tan\beta$ (left); κ_{Agg} as a function of $\tan\beta$ for $m_A = 300$ GeV (middle) and 600 GeV (right), with $y_1 = 0.5$, $\tilde{y}_1 = 1$ and $M_\psi = 800$ GeV (blue), 1000 GeV (green).

where $i, j = 1, 2$ and y_{ij}^ϕ 's are given in Appendix A 2. We take the y_1 and \tilde{y}_1 to be real, enforcing CP invariance in the BSM sector. The relative sign between y_1 and \tilde{y}_1 in Eq. (20) is physical for the following reason. If we want to get rid of this relative sign we need to make the transformations $\chi_L \rightarrow -\chi_L$ and $\chi_R \rightarrow \chi_R$, or $\chi_L \rightarrow \chi_L$ and $\chi_R \rightarrow -\chi_R$. In either case, the M_χ changes its sign and is therefore a physical effect. For chiral fermions, the sign of the mass term is not physical since one can rotate it away by the above transformations.

Instead of the χ [with hypercharge ($Y_\psi - 1/2$)], if we consider a VLF (say ξ) of hypercharge ($Y_\psi + 1/2$), we get a different model where the ξ couples to the $\tilde{\Phi}_1$ instead of the Φ_1 . This model will have similar phenomenology as the $MVQD_{11}$ model, which we discuss later.

The effective couplings for this model are given in Appendix B. When $y_1 = \tilde{y}_1$, in addition to CP invariance, the Lagrangian in Eq. (21) is also invariant under P and C individually, with A transforming as $A \xrightarrow{P} A$, $A \xrightarrow{C} -A$. This implies that the VLF contribution to κ_{AVV} is zero since $AV_{\mu\nu}\tilde{V}^{\mu\nu}$ is not P invariant (although it is CP invariant). Also, the VLF contributions are maximum for $M_\psi = M_\chi$ when the mixing between the VLFs (ψ_2 and χ) is maximum. We will take M_ψ and M_χ to be equal from now on.

In Fig. 16, we plot $BR(A \rightarrow VV)$ for $Y_\psi = 1/6$ as an example, which is the SM quark-doublet hypercharge assignment. The tree level decays to SM fermions $BR(A \rightarrow b\bar{b}, \tau^+\tau^-, t\bar{t})$ are unchanged from what is shown in Fig. 7 for the Type-II 2HDM. We see that for small values of $\tan\beta$ the VLF contribution to $BR(A \rightarrow VV)$ is small compared to the 2HDM-II. This is because y_{ij} 's are proportional to $\sin\beta$. For large $\tan\beta$ and for large m_A , the VLF contributions to the $BR(A \rightarrow \gamma\gamma)$ become significant.

In Fig. 17, we plot contours of κ_{Agg} for $M_\psi = 800$ GeV, 1700 GeV. For comparison we have also plotted the corresponding contours in the 2HDM-II. Using this, one can read off the $\sigma(gg \rightarrow A)$ at the 8 and 14 TeV LHC from Fig. 1 in Sec. II. For comparison, the corresponding contours in the Type-II 2HDM (without the VLFs) are

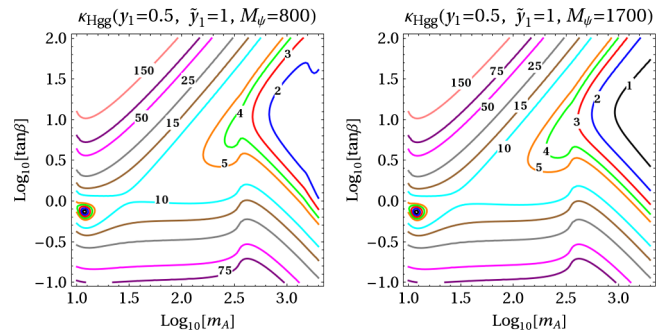


FIG. 19. Contours of κ_{Hgg} for $y_1 = 0.5$, $\tilde{y}_1 = 1$, for $M_\psi = M_\chi = 800$ GeV (left), 1700 GeV (right) for the $MVQD_{11}$ model. The corresponding contours in the Type-II 2HDM are shown in Fig. 8.

shown in Fig. 8. In Fig. 18 (left) we plot y_{11}^h and y_{11}^A [defined in Eq. (24)] in the alignment limit ($\beta - \alpha = \pi/2$), which shows that the h couplings to the VLFs become very small as $\tan\beta$ increases. Thus, the VLFs can modify $\sigma(gg \rightarrow A)$ and $\Gamma(A \rightarrow VV)$ significantly, while the h remains SM-like as required by the LHC measurements of the 125 GeV state. We find that the VLF contributions partially cancel the SM fermion contributions for a range of low $\tan\beta$ values and for some ranges of m_A , while for larger $\tan\beta$ the effective couplings always increase compared to the 2HDM-II. To illustrate this point more explicitly, we plot κ_{Agg} as a function of $\tan\beta$ in Fig. 18 for $m_A = 300$ GeV and 600 GeV. The constraint on the 2HDM was nontrivial only for large $\tan\beta$ (see Fig. 9). Therefore, for large $\tan\beta$, since the κ_{Agg} is bigger for this model compared to the 2HDM (see Fig. 18), and the tree-level $\tau^+\tau^-$ BR from which the tightest constraint appears is almost unchanged, the constraint on this model will be tighter. In Fig. 19, we plot contours of κ_{Hgg} for $m_A = m_H$, in the alignment limit. Corresponding contours in the Type-II 2HDM are shown in Fig. 8. From this, one can also obtain $\sigma(gg \rightarrow H)$ from Fig. 1.

MVQU₂₂ model.—We introduce one doublet VLQ (ψ) with hypercharge Y_ψ and one singlet VLQ (ξ) with hypercharge $Y_\psi + 1/2$, which couples only to Φ_2 . We add the following terms to the 2HDM-II Lagrangian:

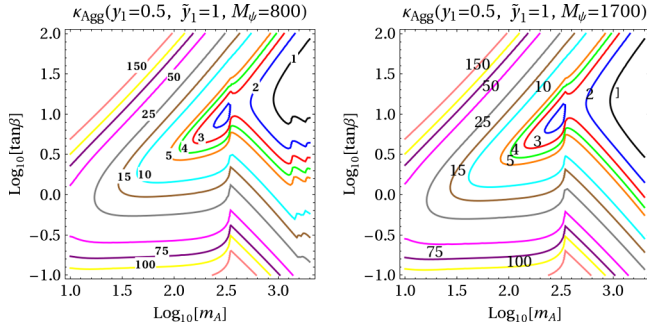


FIG. 20. Contours of $\kappa_{A_{gg}}$ for $y_2 = 0.5$, $\tilde{y}_2 = 1$, for $M_\psi = M_\chi = 800$ GeV (left), 1700 GeV (right) for the $MVQU_{22}$ model.

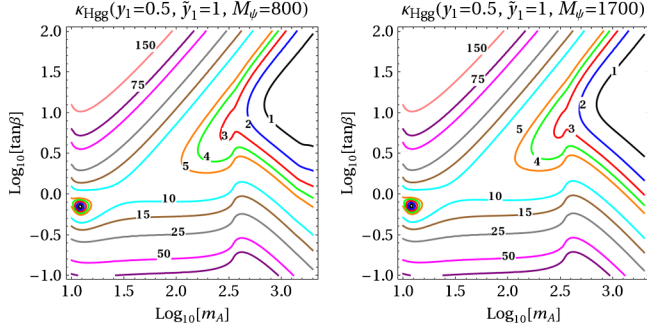


FIG. 21. Contours of $\kappa_{H_{gg}}$ for $y_2 = 0.5$, $\tilde{y}_2 = 1$, for $M_\psi = M_\chi = 800$ GeV (left), 1700 GeV (right) for the $MVQU_{22}$ model.

$$\mathcal{L} \supset \bar{\psi} i \not{D} \psi + \bar{\xi} i \not{D} \xi - y_2 \bar{\psi}_L \tilde{\Phi}_2 \xi_R - \tilde{y}_2 \bar{\psi}_R \tilde{\Phi}_2 \xi_L + \text{H.c.} - M_\psi \bar{\psi} \psi - M_\chi \bar{\xi} \xi. \quad (25)$$

Here we do not include the terms $\bar{\psi}_L \tilde{\Phi}_1 \xi_R$ and $\bar{\psi}_R \tilde{\Phi}_1 \xi_L$ as their effects have been considered in the $MVQD_{11}$ model. As the $\text{BR}(A \rightarrow VV)$ s do not change much compared to the 2HDM-II case, we do not show them here. Instead of the ξ [with hypercharge ($Y_\psi + 1/2$)] if we consider a VLF (say χ) of hypercharge ($Y_\psi - 1/2$) we get a different model where the χ couples to the Φ_2 instead of the $\tilde{\Phi}_2$. This will give similar effects to what we consider here.

Similar to the $MVQD_{11}$ model, we diagonalize the mass matrix by an orthogonal rotation and define the couplings y_{ij}^ϕ . The mass eigenvalues, mixing angles and y_{ij}^ϕ 's for this model can be found in Appendix A 2. The effective couplings for this model are given in Appendix B. As in the $MVQD_{11}$ model, the κ_{AVV} becomes zero when $y_2 = \tilde{y}_2$. In Fig. 20 we plot contours of $\kappa_{A_{gg}}$ in m_A - $\tan\beta$ plane. In the $MVQU_{22}$ model the VLF contributions to $\kappa_{A_{gg}}$ are very small for $y_1 = 0.5$ and $\tilde{y}_1 = 1$, and therefore we do not show it explicitly. This is particularly so for large $\tan\beta$ because the y_{ij} 's are proportional to $\cos\beta$, which become small as $\tan\beta$ increases. Similar conclusions hold for $\kappa_{H_{gg}}$. In Fig. 21 we plot $\kappa_{H_{gg}}$ using which one can read off the $\sigma(gg \rightarrow H)$ from Fig. 1 by reading the $\kappa_{A_{gg}}$ there as $\kappa_{H_{gg}}$, as mentioned earlier. Since $\kappa_{A_{gg}}$ and $\kappa_{H_{gg}}$ do not change much

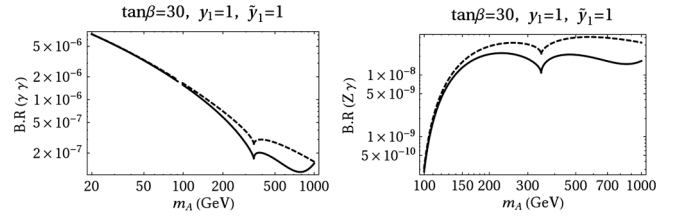


FIG. 22. $\text{BR}(A \rightarrow \gamma\gamma)$ (left) and $\text{BR}(A \rightarrow Z\gamma)$ (right) with $M_\psi = M_\chi = 1000$ GeV for $\tan\beta = 30$ for $MVQU_{12}$ model (solid black), and the corresponding variation in the Type-II 2HDM (dashed black). The BR for $\tan\beta = 1$ and the $\text{BR}(A \rightarrow \tau\tau, bb, tt)$ are not explicitly shown here as they are identical to those in Figs. 16 and 7 respectively.

compared to the 2HDM-II, constraints on the m_A - $\tan\beta$ plane will almost remain the same as in the 2HDM-II case. Thus, VLFs, if realized as in the $MVQU_{22}$ model, have little impact on the observables we consider here.

MVQU₁₂ model.—We introduce one doublet VLQ (ψ) with hypercharge Y_ψ and one singlet VLQ (ξ) with hypercharge ($Y_\psi + 1/2$). We consider the case where ξ_R couples only to Φ_1 and ξ_L couples only to Φ_2 . To the 2HDM-II Lagrangian, we add

$$\mathcal{L} \supset \bar{\psi} i \not{D} \psi + \bar{\xi} i \not{D} \xi - (y_1 \bar{\psi}_L \tilde{\Phi}_1 \xi_R + \tilde{y}_1 \bar{\psi}_R \tilde{\Phi}_2 \xi_L + \text{H.c.}) - M_\psi \bar{\psi} \psi - M_\chi \bar{\xi} \xi. \quad (26)$$

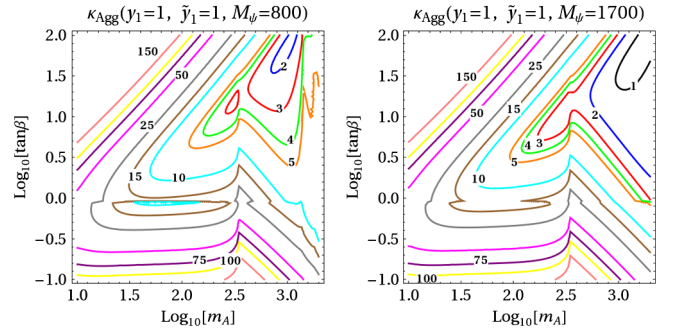


FIG. 23. Contours of $\kappa_{A_{gg}}$ for $y_1 = 1$, $\tilde{y}_1 = 1$, for $M_\psi = M_\chi = 800$ GeV (left) and 1700 GeV (right) for the $MVQU_{12}$ model.

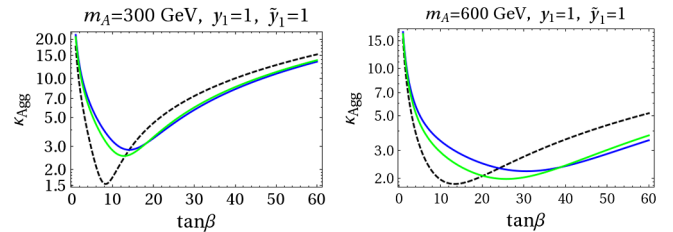


FIG. 24. $\kappa_{A_{gg}}$ with $\tan\beta$ for $m_A = 300$ GeV (left) and 600 GeV (right) with $y_1 = 1$, $\tilde{y}_1 = 1$ and $M_\psi = 800$ GeV (blue), 1000 GeV (green) for the $MVQU_{12}$ model and 2HDM-II (dashed-black).

We get different models if instead of the couplings above, the ψ_R couples to $\tilde{\Phi}_1$ and ψ_L couples to $\tilde{\Phi}_2$, or, if instead of ξ we introduce a VLF singlet (say χ) with hypercharge ($Y_\psi - 1/2$) with couplings to Φ_1 and Φ_2 . All these models have a similar phenomenology as the $MVQU_{12}$ model.

The mass eigenvalues, mixing angles and y_{ij}^ψ 's for this model can be found in Appendix A 3. The effective couplings for this model are given in Appendix B. In this model, the effective couplings do not reduce to zero for $y_1 = \tilde{y}_1$, unlike in the $MVQD_{11}$ and $MVQU_{22}$ models, as there are no additional P and C symmetries in the VLF sector. In Fig. 22, we plot the $\text{BR}(A \rightarrow VV)$, $\text{BR}(A \rightarrow b\bar{b}, \tau^+\tau^-, t\bar{t})$ for an example choice of $Y_\psi = 1/6$. The $\text{BR}(A \rightarrow \gamma\gamma, Z\gamma)$ for $\tan\beta = 1$, $y_1 = 0.5$, $\tilde{y}_1 = 1$ and the tree-level $\text{BR}(A \rightarrow \tau\tau, bb, tt)$ are not explicitly shown in Fig. 22 as they are identical to those shown for the $MVQD_{11}$ model in Fig. 16 and the Type-II 2HDM in Fig. 7. In Fig. 23 we plot contours of $\kappa_{A_{gg}}$ for $y_1 = \tilde{y}_1 = 1$ and $M_\psi = M_\xi = 800$ GeV and 1700 GeV. From this, one can obtain $\sigma(gg \rightarrow A)$ at the 8 and 14 TeV LHC from Fig. 1 in Sec. II. For low values of $\tan\beta$ the effective coupling increases compared to the 2HDM-II case, while for larger values of $\tan\beta$ the effective coupling decreases compared to the 2HDM-II. To show this more explicitly, we plot $\kappa_{A_{gg}}$ with $\tan\beta$ in Fig. 24. The decreased coupling is due to a destructive interference between the contributions from SM

fermions and the VLFs. If we reverse the sign of y_1 or \tilde{y}_1 , we get the opposite effect; for low values of $\tan\beta$ the effective coupling decreases compared to the 2HDM-II while for larger values of $\tan\beta$ the effective coupling increases compared to the 2HDM-II. In Fig. 25 we plot contours of $\kappa_{H_{gg}}$ in the alignment limit. From this, one can also obtain $\sigma(gg \rightarrow H)$ from Fig. 1 by reading $\kappa_{A_{gg}}$ there as $\kappa_{H_{gg}}$, as mentioned earlier.

In Fig. 26 we plot the region of the m_A - $\tan\beta$ parameter space which is excluded at the 95% confidence level for two cases: when only A is present, and when A and H are degenerate and both present. For comparison, we have also plotted the corresponding limit for the 2HDM-II case. We see that the constraints are loosened compared to the 2HDM-II due to the presence of VLFs. This happens because of the reduction of $\kappa_{A_{gg}}$ ($\kappa_{H_{gg}}$) compared to the 2HDM-II.

Next, we add VLFs to the Type-X 2HDM and study the phenomenology of the neutral scalars.

5. Type-X 2HDM with VLQ-VLQ Yukawa couplings

MVQDX₁₁ model.—To the 2HDM Type-X model in Eq. (11), we introduce VLFs in a similar fashion as in the $MVQD_{11}$ model, as a representative case, and call it $MVQDX_{11}$ model. The other ways of coupling VLFs similar to the $MVQU_{22}$ or $MVQU_{12}$ model will be qualitatively similar to our results here. We introduce a

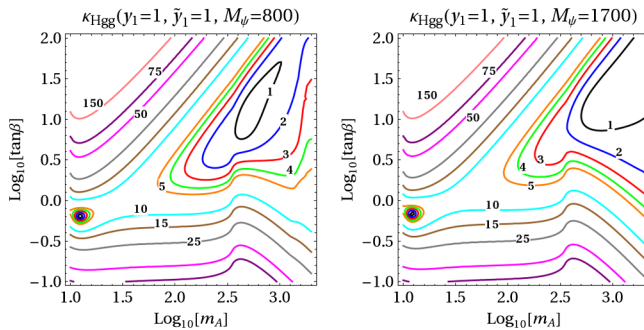


FIG. 25. Contours of $\kappa_{H_{gg}}$ for $y_1 = 1$, $\tilde{y}_1 = 1$, for $M_\psi = M_\chi = 800$ GeV (left), 1700 GeV (right) for the $MVQU_{12}$ model.

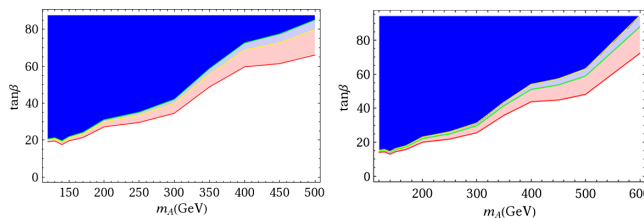


FIG. 26. For the $MVQU_{12}$ model, regions of the m_A - $\tan\beta$ parameter space excluded at the 95% C.L. from $\phi \rightarrow \tau^+\tau^-$ decay when only A is present (left), and when A and H are degenerate and both present (right), with $y_1 = \tilde{y}_1 = 1$, $M_\psi = M_\chi = 800$ GeV (dark blue region), 1000 GeV (light blue and dark blue regions). All shaded regions are excluded in the 2HDM-II.

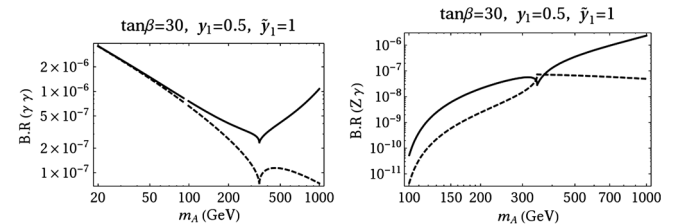


FIG. 27. $\text{BR}(A \rightarrow \gamma\gamma, Z\gamma)$ with $M_\psi = M_\chi = 1000$ GeV (solid black) for $\tan\beta = 30$ for the $MVQDX_{11}$ model, and the corresponding variation in the 2HDM-X (dashed black).

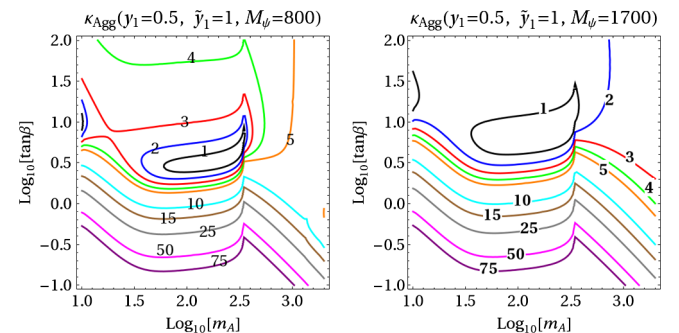


FIG. 28. Contours of $\kappa_{A_{gg}}$ for $y_1 = 0.5$, $\tilde{y}_1 = 1$, for $M_\psi = M_\chi = 800$ GeV (left), 1700 GeV (right) for the $MVQDX_{11}$ model. The corresponding contours in the Type-X 2HDM is shown in Fig. 11.

doublet VLQ $\psi = (\psi_1, \psi_2)$ with hypercharge Y_ψ , and a singlet VLQ (χ) with hypercharge ($Y_\psi - 1/2$) which couples only to Φ_1 . To the 2HDM-X Lagrangian we add

$$\mathcal{L} \supset \bar{\psi} i \not{D} \psi + \bar{\chi} i \not{D} \chi - (y_1 \bar{\psi}_L \Phi_1 \chi_R + \tilde{y}_1 \bar{\psi}_R \Phi_1 \chi_L + \text{H.c.}) - M_\psi \bar{\psi} \psi - M_\chi \bar{\chi} \chi. \quad (27)$$

The effective couplings of A with VLFs are same as in the $MVQD_{11}$ model and can be read off from Appendix B. In Fig. 27 we show $\text{BR}(A \rightarrow VV)$ including the VLF contributions for the $MVQDX_{11}$ model; the tree-level $\text{BR}(A \rightarrow \tau^+ \tau^-, b\bar{b}, t\bar{t})$ is unchanged from what are shown in Fig. 10. $\text{BR}(A \rightarrow \gamma\gamma, Z\gamma)$ for $\tan\beta = 1, y_1 = 0.5, \tilde{y}_1 = 1$ are almost identical to the 2HDM values shown in Fig. 16 and are therefore not shown explicitly in Fig. 27. For $\tan\beta = 30$, $\text{BR}(A \rightarrow \gamma\gamma, Z\gamma)$ is increased compared to 2HDM-II, because for large $\tan\beta$, $\Gamma(A \rightarrow b\bar{b})$ becomes much smaller in 2HDM-X.

In Fig. 28 we plot contours of $\kappa_{A\text{agg}}$. The $\kappa_{\phi gg}$ contours in 2HDM-X (without VLFs) are shown in Fig. 11. Using these plots, one can read off $\sigma(gg \rightarrow A)$ for 8 TeV and 14 TeV LHC from Fig. 1 in Sec. II. As expected, for large $\tan\beta$, $\kappa_{A\text{agg}}$ is significantly larger in this model compared to 2HDM-X since the VLFs contribute substantially while the SM quark contributions alone are very small. In order to

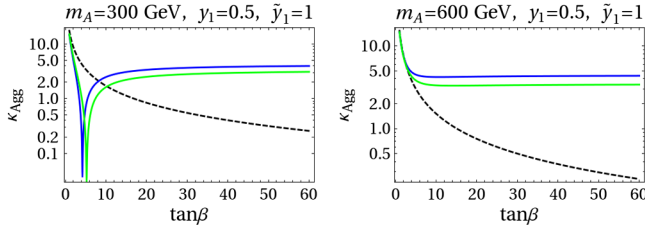


FIG. 29. $\kappa_{A\text{agg}}$ with $\tan\beta$ for $m_A = 300$ GeV (left) and 600 GeV (right) with $y_1 = 0.5, \tilde{y}_1 = 1$ and $M_\psi = 800$ GeV (blue), 1000 GeV (green) for the $MVQDX_{11}$ model and the 2HDM-X (dashed black).

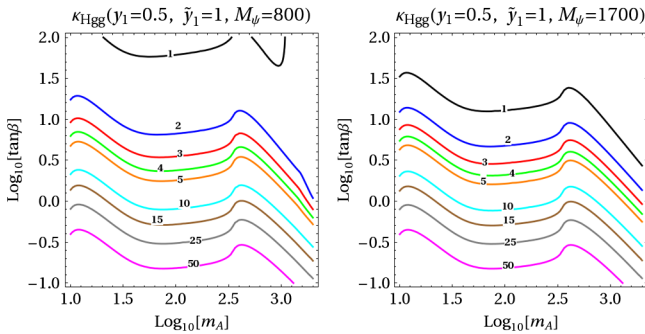


FIG. 30. Contours of $\kappa_{H\text{agg}}$ for $y_1 = 0.5, \tilde{y}_1 = 1$, for $M_\psi = M_\chi = 800$ GeV (left), 1700 GeV (right) for the $MVQDX_{11}$ model. The corresponding contours in the Type-X 2HDM is shown in Fig. 11.

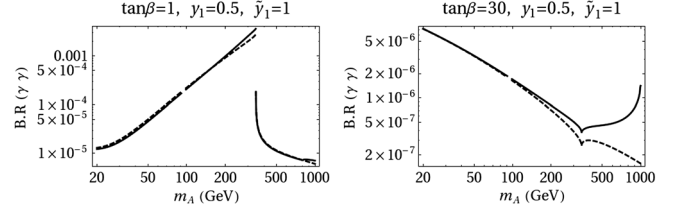


FIG. 31. $\text{BR}(A \rightarrow \gamma\gamma)$ with $M_\psi = M_\chi = 500$ GeV, $y_1 = 0.5, \tilde{y}_1 = 1$ for $\tan\beta = 1$ (left) and $\tan\beta = 30$ (right) for the $MVLE_{11}$ model.

show explicitly how large the change is, we plot $\kappa_{A\text{agg}}$ as a function of $\tan\beta$ for $m_A = 300$ GeV and 600 GeV in Fig. 29. In Fig. 30 we plot contours of $\kappa_{H\text{agg}}$ in the m_A - $\tan\beta$ plane in the alignment limit. From this, one can also obtain $\sigma(gg \rightarrow H)$ from Fig. 1.

6. Type-II 2HDM with VLL-VLL Yukawa couplings

MVLE₁₁ model.—Vectorlike leptons do not contribute in $gg \rightarrow A$, but can contribute in $A \rightarrow \gamma\gamma, Z\gamma$. We show the effect of VLLs in a simple model similar to the $MVQD_{11}$ model, but with VLLs instead of VLQs. We introduce one doublet VLL (ψ) with hypercharge Y_ψ and one singlet VLL (χ) with hypercharge ($Y_\psi - 1/2$). The Lagrangian we consider is exactly the same as in Eq. (20), except here the VLLs ψ and χ do not couple to gluons. The effective couplings are the same as for the $MVQD_{11}$ model except for color factors. As an example, we choose $Y_\psi = -1/2$ and plot $\text{BR}(A \rightarrow \gamma\gamma)$ as a function of m_A in Fig. 31, with $M_\psi = M_\chi = 500$ GeV, for $\tan\beta = 1$ and 30. We see that the effect of VLLs is qualitatively similar to vectorlike quarks; for low $\tan\beta$ the effect of VLLs is negligible while for large $\tan\beta$ and large m_A VLL contributions are significant. Near $m_A = 1000$ GeV, the VLL contribution is quite large due to them going on shell for our choice of VLL mass of 500 GeV. $\text{BR}(A \rightarrow Z\gamma)$ will show the same behavior.

IV. CONCLUSIONS

Many theories beyond the standard model contain new CP -odd and CP -even neutral scalars $\phi = \{A, H\}$ and new vectorlike fermions (ψ_{VL}). We study the LHC phenomenology of ϕ taking into account ψ_{VL} contributions to $\phi gg, \phi\gamma\gamma$ and $\phi Z\gamma$ couplings at the 1-loop level.

In Sec. II we write an effective Lagrangian with ϕ coupled to SM gauge bosons and fermions. We focus only on ϕ Yukawa couplings to third-generation SM fermions, namely t, b, τ , since these are usually the bigger couplings in most BSM extensions. The couplings of the A to standard model W, Z gauge bosons (i.e. AVV couplings) cannot occur from renormalizable operators in a CP -conserving sector, but can be induced as loop-generated nonrenormalizable operators. These operators are induced by SM fermions and also the heavy ψ_{VL} . In Sec. II we

present model-independent results that are useful whatever the origin of these effective couplings. In Fig. 1 we present the 8 TeV and 14 TeV LHC $gg \rightarrow \phi$ (gluon-fusion channel) cross sections as a function of the effective couplings. We also obtain limits on the effective couplings from the 8 TeV LHC data on the $\gamma\gamma$, $\tau^+\tau^-$ and $t\bar{t}$ modes. We do not include the $b\bar{b}$ decay mode and the b -quark associated production channels in this work.

We define some simple models in Sec. III that are representative of BSM constructions as far as the phenomenology of ϕ is concerned. These models include ϕ and ψ_{VL} in the singlet and doublet representations of $SU(2)$. In the doublet case, we focus on the 2HDM Type-II and Type-X models. We compute the ϕgg , $\phi\gamma\gamma$ and $\phi Z\gamma$ effective couplings induced by the SM fermions and vectorlike fermions at the 1-loop level and present analytical expressions for them in Appendix A. For the various models we define, we present the effective couplings $\kappa_{\phi gg}$, $\kappa_{\phi\gamma\gamma}$, $\kappa_{\phi Z\gamma}$, and $\text{BR}(A \rightarrow \gamma\gamma, Z\gamma)$ and $\text{BR}(A \rightarrow f\bar{f})$ for $f = \{\tau, b, t\}$ as a function of the model parameters. From the $\kappa_{\phi gg}$ and the BR into one of these modes, one can see if a point in parameter space in a given model is allowed by the 8 TeV data from our plots in Sec. II. One can also read off the gluon-fusion cross section at the 8 TeV and 14 TeV LHC from Fig. 1. Interestingly, for some of the 2HDM cases we studied, we find that the addition of vectorlike fermions loosens the constraint compared to the 2HDM alone, and allows more of the parameter space. This can be seen for instance in Fig. 26. The 14 TeV LHC gluon-fusion CS of the ϕ and its BRs in the different models we present should be useful in identifying allowed regions of parameter space and promising discovery channels of the ϕ . In this context, it is interesting to explore the possibility of the ϕ being the state responsible for the recent 750 GeV excess of diphoton events at the 13 TeV LHC [57,58]; this is the subject of a separate work.

ACKNOWLEDGMENTS

We thank Gautam Bhattacharya and Dipankar Das for a discussion on the unitarity bounds in 2HDM, and V. Ravindran for a discussion on $b\bar{b}$ fusion.

APPENDIX A: COUPLINGS, MASSES AND MIXING ANGLES IN VARIOUS MODELS

Here we provide the explicit expressions for the mixing angles and the mass eigenvalues in the different models we have defined in Sec. III. We also provide expressions for the κ_{ij} 's, y_{ij} 's defined in Eq. (24). Sec. A 1 contains the mixing angles and the mass eigenvalues for the MVU , MVD and MVQ models. Sec. A 2 contains explicit expressions for y_{ij} 's and κ_{ij} 's for the $MVQD_{11}$, $MVQU_{22}$ and $MVQDX_{11}$ models. Sec. A 3 contains explicit expressions for y_{ij} 's and κ_{ij} 's for the $MVQU_{12}$ model. In what follows we will use the notations $c_{L,R} = \cos\theta_{L,R}$, $s_{L,R} = \sin\theta_{L,R}$, $c_\beta = \cos\beta$ and $s_\beta = \sin\beta$.

1. MVU , MVD , MVQ models

In this section we give the mixing angles and the mass eigenvalues for the MVU , MVD and MVQ models. The mixing angles $\theta_{L,R}^U$, for MVU model are given by

$$\begin{aligned}\tan 2\theta_L^U &= \frac{2\sqrt{2}y_1v_1M_\psi}{y_u^2v_2^2 - 2M_\psi^2 + y_1^2v_1^2}, \\ \tan 2\theta_R^U &= \frac{2\sqrt{2}y_1y_u v_1 v_2}{y_u^2v_2^2 - 2M_\psi^2 - y_1^2v_1^2}.\end{aligned}\quad (\text{A1})$$

The mass eigenvalues for the EM charge-2/3 fermions in MVU model are given by

$$m_{t,t_2} = \frac{1}{2} \left(\sqrt{\left(\frac{y_u}{\sqrt{2}}v_2 + M_\psi\right)^2 + \frac{y_1^2}{2}v_1^2} \mp \sqrt{\left(\frac{y_u}{\sqrt{2}}v_2 - M_\psi\right)^2 + \frac{y_1^2}{2}v_1^2} \right). \quad (\text{A2})$$

The mixing angle and mass eigenvalues for the MVD model are obtained from Eq. (A1) and Eq. (A2) by the replacements $y_1 \rightarrow y_2$, $y_u v_2 \rightarrow y_d v_1$ and $M_\psi \rightarrow M_\chi$. The mixing angles $\theta_{L,R}^U$, for the MVQ model are given by

$$\tan 2\theta_R^U = \frac{2\sqrt{2}\tilde{y}_1^{\text{eff}}v_2M_Q^{\text{eff}}}{2(M_Q^{\text{eff}})^2 - (y_u^{\text{eff}})^2v_2^2 + (\tilde{y}_1^{\text{eff}})^2v_2^2}, \quad \tan 2\theta_L^U = \frac{2\sqrt{2}\tilde{y}_1^{\text{eff}}y_u^{\text{eff}}v_2^2}{2(M_Q^{\text{eff}})^2 - (y_u^{\text{eff}})^2v_2^2 - (\tilde{y}_1^{\text{eff}})^2v_2^2}.$$

The mass eigenvalues for the EM charge-2/3 fermions in the MVQ model are given by

$$m_{t,t_2} = \frac{1}{2} \left(\sqrt{\left(\frac{y_u^{\text{eff}}}{\sqrt{2}}v_2 + M_Q^{\text{eff}}\right)^2 + \frac{(\tilde{y}_1^{\text{eff}})^2}{2}v_2^2} \mp \sqrt{\left(\frac{y_u^{\text{eff}}}{\sqrt{2}}v_2 - M_Q^{\text{eff}}\right)^2 + \frac{(\tilde{y}_1^{\text{eff}})^2}{2}v_2^2} \right).$$

2. $MVQD_{11}$, $MVQU_{22}$ models

In this section we give the expressions for the y_{ij} 's and κ_{ij} 's for the $MVQD_{11}$, $MVQU_{22}$ models. The couplings κ_{ij} defined in Eq. (24) for the $MVQD_{11}$, $MVQU_{22}$ models and also for the $MVQDX_{11}$ model are given by $\kappa_{11} = (g/c_W) \times [(T^3/2)(c_L^2 + c_R^2) - Qs_W^2]$, $\kappa_{22} = (g/c_W) [(T^3/2)(s_L^2 + s_R^2) - Qs_W^2]$, $\kappa_{12} = -(g/c_W)(T^3/2)(s_L c_L + s_R c_R)$. The mass eigenvalues $M_{1,2}$ [in Eq. (24)] for the $MVQD_{11}$ model are given by

$$M_{1,2} = \frac{1}{2} \sqrt{(M_\psi + M_\chi)^2 + \frac{1}{2} c_\beta^2 v^2 (y_1 - \tilde{y}_1)^2} \pm \sqrt{(M_\psi - M_\chi)^2 + \frac{1}{2} v^2 c_\beta^2 (y_1 + \tilde{y}_1)^2} \quad (\text{A3})$$

and the mixing angles $\theta_{L,R}$ for $MVQD_{11}$ model are given by

$$\tan 2\theta_L = \frac{2\sqrt{2}vc_\beta(y_1 M_\chi + \tilde{y}_1 M_\psi)}{2(M_\psi^2 - M_\chi^2) - v^2 c_\beta^2 (\tilde{y}_1^2 - y_1^2)},$$

$$\tan 2\theta_R = \frac{2\sqrt{2}vc_\beta(y_1 M_\chi + \tilde{y}_1 M_\psi)}{2(M_\psi^2 - M_\chi^2) + v^2 c_\beta^2 (\tilde{y}_1^2 - y_1^2)}. \quad (\text{A4})$$

The mass eigenvalues and the mixing angles for $MVQU_{22}$ model can be obtained from Eqs. (A3) and (A4) by the

replacements $y_1 \rightarrow y_2$ and $c_\beta \rightarrow s_\beta$. The couplings y_{ij}^A 's [in Eq. (24)] for the $MVQD_{11}$ model are given by $y_{11}^A = (1/\sqrt{2})s_\beta(-y_1 c_L s_R + \tilde{y}_1 s_L c_R)$, $y_{22}^A = (1/\sqrt{2})s_\beta(y_1 s_L c_R - \tilde{y}_1 c_L s_R)$, $y_{12}^A = -(1/\sqrt{2})s_\beta(y_1 c_L c_R + \tilde{y}_1 s_L s_R)$, $y_{21}^A = (1/\sqrt{2})s_\beta(y_1 s_L s_R + \tilde{y}_1 c_L c_R)$. The y_{ij}^A 's in the $MVQU_{22}$ model can be obtained from the y_{ij}^A 's in the $MVQD_{11}$ model by the replacements $y_1 \rightarrow y_2$ and $s_\beta \rightarrow c_\beta$. The couplings y_{ij}^h [in Eq. (24)] are given by $y_{11}^h = -(1/\sqrt{2})s_\alpha \times (y_1 c_L s_R + \tilde{y}_1 s_L c_R)$, $y_{22}^h = (1/\sqrt{2})s_\alpha(y_1 s_L c_R + \tilde{y}_1 c_L s_R)$, $y_{12}^h = -(1/\sqrt{2})s_\alpha(y_1 c_L c_R - \tilde{y}_1 s_L c_R)$, $y_{21}^h = -(1/\sqrt{2})s_\alpha \times (-y_1 s_L s_R + \tilde{y}_1 c_L c_R)$. The y_{ij}^h 's in the $MVQU_{22}$ model can be obtained from y_{ij}^h 's in the $MVQD_{11}$ model by the replacements $y_1 \rightarrow y_2$ and $s_\alpha \rightarrow -c_\alpha$. The couplings y_{ij}^H [in Eq. (24)] can be obtained from the y_{ij}^h 's in the $MVQD_{11}$ model by the replacements $s_\alpha \rightarrow -c_\alpha$ in case of $MVQD_{11}$ and $s_\alpha \rightarrow -s_\alpha$ for the $MVQU_{22}$ model.

3. $MVQU_{12}$ model

In this section we give the expressions for the y_{ij} 's and κ_{ij} 's for the $MVQU_{12}$ model. The couplings κ_{ij} for the $MVQU_{12}$ model are same as in the $MVQD_{11}$ model. The mass eigenvalues are given by

$$M_{1,2} = \frac{1}{2} \sqrt{(M_\psi + M_\xi)^2 + \frac{1}{2} v^2 (y_1 c_\beta - \tilde{y}_1 s_\beta)^2} \pm \sqrt{(M_\psi - M_\xi)^2 + \frac{1}{2} v^2 (y_1 c_\beta + \tilde{y}_1 s_\beta)^2}. \quad (\text{A5})$$

and the mixing angles $\theta_{L,R}$ are given by

$$\tan 2\theta_L = \frac{2\sqrt{2}v(y_1 c_\beta M_\xi + \tilde{y}_1 s_\beta M_\psi)}{2(M_\psi^2 - M_\xi^2) - v^2 (\tilde{y}_1^2 s_\beta^2 - y_1^2 c_\beta^2)}, \quad \tan 2\theta_R = \frac{2\sqrt{2}v(y_1 c_\beta M_\xi + \tilde{y}_1 s_\beta M_\psi)}{2(M_\psi^2 - M_\xi^2) + v^2 (\tilde{y}_1^2 s_\beta^2 - y_1^2 c_\beta^2)}. \quad (\text{A6})$$

The couplings y_{ij}^A are given by $y_{11}^A = (1/\sqrt{2})(y_1 s_\beta c_L s_R + \tilde{y}_1 c_\beta s_L c_R)$, $y_{22}^A = -(1/\sqrt{2})(y_1 s_\beta s_L c_R + \tilde{y}_1 c_\beta c_L s_R)$, $y_{12}^A = (1/\sqrt{2})(y_1 s_\beta c_L c_R - \tilde{y}_1 c_\beta s_L s_R)$, $y_{21}^A = -(1/\sqrt{2})(y_1 s_\beta s_L s_R - \tilde{y}_1 c_\beta c_L c_R)$. The couplings y_{ij}^h are given by $y_{11}^h = (1/\sqrt{2})(-y_1 s_\alpha c_L s_R + \tilde{y}_1 c_\alpha s_L c_R)$, $y_{22}^h = (1/\sqrt{2})(y_1 s_\alpha s_L c_R - \tilde{y}_1 c_\alpha c_L s_R)$, $y_{12}^h = -(1/\sqrt{2})(y_1 s_\alpha c_L c_R + \tilde{y}_1 c_\alpha s_L s_R)$, $y_{21}^h = (1/\sqrt{2})(y_1 s_\alpha s_L s_R + \tilde{y}_1 c_\alpha c_L c_R)$. The y_{ij}^H 's can be obtained from y_{ij}^h 's by the replacements $s_\alpha \rightarrow -c_\alpha$ and $c_\alpha \rightarrow s_\alpha$.

APPENDIX B: THE $\kappa_{\phi gg, \phi \gamma \gamma, \phi Z \gamma, AWW, AZZ}$ EFFECTIVE COUPLINGS IN VARIOUS MODELS

In this section we give the expressions for the $\kappa_{\{\phi gg, \phi \gamma \gamma, \phi Z \gamma, AWW, AZZ\}}$ in the various models we considered in Sec. III.

1. $\kappa_{\phi gg}, \kappa_{\phi \gamma \gamma}$

The 1-loop expressions for the ϕgg and $\phi \gamma \gamma$ amplitudes $\kappa_{\phi gg}$ and $\kappa_{\phi \gamma \gamma}$ respectively, with

$\phi = \{h, H, A\}$, are given here. These amplitudes are induced by quarks whose effective Lagrangian can be written as $\mathcal{L}_\phi^f \supset m_f \bar{f} f + y_{\phi f f} \phi \bar{f} f$. Defining $r_f = m_f^2/m_\phi^2$ and with f running over all colored fermion species with mass m_f and Yukawa couplings $y_{\phi f f}$, and with the electric charge of the fermion (f) denoted by Q_f , the general expressions for $\kappa_{\phi gg}$ and $\kappa_{\phi \gamma \gamma}$ are given as

$$\begin{aligned}\kappa_{\phi\gamma\gamma} &= 2e^2 \sum_f N_c^f Q_f^2 y_{\phi ff} \frac{M}{m_f} F_{1/2}^{(1)}(r_f), \\ \kappa_{\phi gg} &= g_s^2 \sum_f y_{\phi ff} \frac{M}{m_f} F_{1/2}^{(1)}(r_f), \quad \text{with} \\ F_{1/2}^{(1)}(r_f) &= 4r_f \left(\int_0^1 dy \int_0^{1-y} dx \frac{g(x,y)}{(r_f - xy)} \right),\end{aligned}\quad (\text{B1})$$

and $g(x,y) = (1 - 4xy)$ for the CP -even scalars (h , H) and 1 for the CP -odd scalar (A). Here M is a mass scale defined in Eq. (1), which we set to 1 TeV for numerical results. Compared to $\kappa_{\phi\gamma\gamma}$, $\kappa_{\phi gg}$ has an extra factor of $1/2$ which compensates for our definition of $\Gamma(\phi \rightarrow gg)$ in Eq. (2) with a relative factor of 8 compared to $\Gamma(\phi \rightarrow \gamma\gamma)$ while the actual color factor is really 2. The expressions for $F_{1/2}^{(1)}$ in Eq. (B1) match with the closed form expressions given in Ref. [59].

2. $\kappa_{AZ\gamma}$

Here we give the general expressions for $\kappa_{AZ\gamma}$ [defined in Eq. (1)] for the different models we have considered. For the SVU and SVQ models,

$$\kappa_{AZ\gamma} = 2e \frac{g}{c_W} \sum_i N_c^i Q_i (T_3^i - Q_i s_W^2) y_A \frac{M}{m_i} F_{1/2}^{(2)}(r_i, r_Z),$$

with

$$F_{1/2}^{(2)}(r_i, r_Z) = 4r_i \int_0^1 dy \int_0^{1-y} dx \frac{1}{r_i + (r_Z - 1)xy + r_Z(x^2 - x)}.$$

For the SVU model, only one VLF contributes to $\kappa_{AZ\gamma}$. For the $MVQD_{11}$, $MVQU_{22}$, $MVQU_{12}$ and $MVQDX_{11}$ models, $\kappa_{AZ\gamma} = \kappa_{AZ\gamma}^1 + \kappa_{AZ\gamma}^2 + \kappa_{AZ\gamma}^{12} + \kappa_{AZ\gamma}^{21}$, where

$$\begin{aligned}\kappa_{AZ\gamma}^i &= 2e N_c^i Q_i \kappa_{ii} y_{ii} \frac{M}{m_i} F_{1/2}^{(2)}(r_i, r_Z), \\ \kappa_{AZ\gamma}^{ij} &= 2e N_c^i Q_i \kappa_{ij} y_{ij} \left(\int_0^1 dy \int_0^{1-y} dx \right. \\ &\quad \left. \times \frac{4M \left(\frac{r_i}{m_i} - \left(\frac{r_i}{m_i} - \frac{r_j}{m_j} \right) x \right)}{r_i(1-x) + r_j x + (r_Z - 1)xy + r_Z(x^2 - x)} \right).\end{aligned}$$

The couplings κ_{ij} , y_{ij} for each of the four cases are given in Appendix A. The expression for $F_{1/2}^{(2)}$ is a generalization to vectorlike fermions of the expression given in Ref. [59].

3. κ_{AZZ} , $\kappa_{A\bar{W}W}$

Here we provide the expressions for κ_{AZZ} and $\kappa_{A\bar{W}W}$ for the SVU and SVQ models. For the SVU and SVQ models,

$$\kappa_{AZZ} = 2 \left(\frac{g}{c_W} \right)^2 \sum_i N_c^i (T_3^i - Q_i s_W^2)^2 y_A \frac{M}{m_i} F_{1/2}^{(3)}(r_i, r_Z),$$

where

$$F_{1/2}^{(3)}(r_i, r_Z) = 4 \int_0^1 dy \int_0^{1-y} dx \frac{r_i}{r_i - xy + r_Z[(x+y)^2 - (x+y)]}.$$

For the SVQ model, $\kappa_{A\bar{W}W} = 2 \left(\frac{g}{\sqrt{2}} \right)^2 \sum_i N_c^i y_A \frac{M}{m_i} F_{1/2}^{(3)}(r_i, r_W)$. For the SVU model, $\kappa_{A\bar{W}W}$ is zero.

-
- [1] R. K. Kaul, arXiv:0803.0381; G. Bhattacharyya, *Rep. Prog. Phys.* **74**, 026201 (2011).
 [2] M. Schmaltz and D. Tucker-Smith, *Annu. Rev. Nucl. Part. Sci.* **55**, 229 (2005); M. Perelstein, *Prog. Part. Nucl. Phys.* **58**, 247 (2007).
 [3] R. Contino, arXiv:1005.4269.
 [4] H. Davoudiasl, S. Gopalakrishna, E. Ponton, and J. Santiago, *New J. Phys.* **12**, 075011 (2010).
 [5] S. Gopalakrishna, T. Mandal, S. Mitra, and R. Tibrewala, *Phys. Rev. D* **84**, 055001 (2011); S. Gopalakrishna, T. Mandal, S. Mitra, and G. Moreau, *J. High Energy Phys.* **08** (2014) 079.
 [6] L. Bento and G. C. Branco, *Phys. Lett. B* **245**, 599 (1990); L. Bento, G. C. Branco, and P. A. Parada, *Phys. Lett. B* **267**, 95 (1991); G. C. Branco, P. A. Parada, and M. N. Rebelo, arXiv:hep-ph/0307119.
 [7] S. A. R. Ellis, R. M. Godbole, S. Gopalakrishna, and J. D. Wells, *J. High Energy Phys.* **09** (2014) 130.
 [8] J. F. Gunion and H. E. Haber, *Phys. Rev. D* **67**, 075019 (2003).
 [9] G. Bhattacharyya and D. Das, arXiv:1507.06424.
 [10] S. Gopalakrishna, T. S. Mukherjee, and S. Sadhukhan, arXiv:1512.05731.
 [11] I. Low, W. Skiba, and D. Tucker-Smith, *Phys. Rev. D* **66**, 072001 (2002).
 [12] S. Liebler, *Eur. Phys. J. C* **75**, 210 (2015).
 [13] E. Bagnaschi, R. V. Harlander, S. Liebler, H. Mantler, P. Slavich, and A. Vicini, *J. High Energy Phys.* **06** (2014) 167.
 [14] B. Coleppa, K. Kumar, and H. E. Logan, *Phys. Rev. D* **86**, 075022 (2012).
 [15] G. Burdman, C. E. F. Haluch, and R. D. Matheus, *Phys. Rev. D* **85**, 095016 (2012).
 [16] B. Dumont, J. F. Gunion, Y. Jiang, and S. Kraml, *Phys. Rev. D* **90**, 035021 (2014).
 [17] B. Dumont, J. F. Gunion, Y. Jiang, and S. Kraml, arXiv:1409.4088.
 [18] K. Cheung, J. S. Lee, and P. Y. Tseng, *J. High Energy Phys.* **01** (2014) 085.
 [19] B. Coleppa, F. Kling, and S. Su, *J. High Energy Phys.* **01** (2014) 161.

- [20] D. Das, *Int. J. Mod. Phys. A* **30**, 1550158 (2015).
- [21] G. Bhattacharyya, D. Das, P. B. Pal, and M. N. Rebelo, *J. High Energy Phys.* **10** (2013) 081.
- [22] K. Cheung, J. S. Lee, E. Senaha, and P. Y. Tseng, *J. High Energy Phys.* **06** (2014) 149.
- [23] A. Broggio, E. J. Chun, M. Passera, K. M. Patel, and S. K. Vempati, *J. High Energy Phys.* **11** (2014) 058.
- [24] C. Y. Chen, S. Dawson, and M. Sher, *Phys. Rev. D* **88**, 015018 (2013).
- [25] A. Drozd, B. Grzadkowski, J. F. Gunion, and Y. Jiang, *J. High Energy Phys.* **05** (2013) 072.
- [26] B. Grinstein and P. Uttayarat, *J. High Energy Phys.* **06** (2013) 094; **09** (2013) 110(E).
- [27] A. Celis, V. Ilisie, and A. Pich, *J. High Energy Phys.* **07** (2013) 053.
- [28] S. Chang, S. K. Kang, J. P. Lee, K. Y. Lee, S. C. Park, and J. Song, *J. High Energy Phys.* **05** (2013) 075.
- [29] O. Eberhardt, U. Nierste, and M. Wiebusch, *J. High Energy Phys.* **07** (2013) 118.
- [30] B. Coleppa, F. Kling, and S. Su, *J. High Energy Phys.* **09** (2014) 161.
- [31] P. S. Bhupal Dev and A. Pilaftsis, *J. High Energy Phys.* **12** (2014) 024; **11** (2015) 147.
- [32] J. Baglio, O. Eberhardt, U. Nierste, and M. Wiebusch, *Phys. Rev. D* **90**, 015008 (2014).
- [33] W. Bernreuther, P. Gonzalez, and M. Wiebusch, *Eur. Phys. J. C* **69**, 31 (2010).
- [34] W. Bernreuther, P. Gonzalez, and M. Wiebusch, arXiv:0909.3772.
- [35] J. de Blas, M. Chala, M. Perez-Victoria, and J. Santiago, *J. High Energy Phys.* **04** (2015) 078.
- [36] F. del Aguila, M. Perez-Victoria, and J. Santiago, *J. High Energy Phys.* **09** (2000) 011; J. A. Aguilar-Saavedra, *J. High Energy Phys.* **11** (2009) 030; J. A. Aguilar-Saavedra, R. Benbrik, S. Heinemeyer, and M. Pérez-Victoria, *Phys. Rev. D* **88**, 094010 (2013); F. del Aguila, J. de Blas, and M. Perez-Victoria, *Phys. Rev. D* **78**, 013010 (2008); F. del Aguila and J. A. Aguilar-Saavedra, *Nucl. Phys.* **B813**, 22 (2009).
- [37] CMS Collaboration, Report No. CMS-PAS-HIG-14-006.
- [38] G. Aad *et al.* (ATLAS Collaboration), *J. High Energy Phys.* **11** (2014) 056.
- [39] G. Aad *et al.* (ATLAS Collaboration), *J. High Energy Phys.* **08** (2015) 148.
- [40] F. Maltoni, Z. Sullivan, and S. Willenbrock, *Phys. Rev. D* **67**, 093005 (2003).
- [41] J. Kozaczuk and T. A. W. Martin, *J. High Energy Phys.* **04** (2015) 046.
- [42] S. Chatrchyan *et al.* (CMS Collaboration), *Phys. Lett. B* **722**, 207 (2013).
- [43] G. Aad *et al.* (ATLAS Collaboration), *J. High Energy Phys.* **01** (2015) 069.
- [44] CMS Collaboration, Report No. CMS-PAS-HIG-14-030.
- [45] J. Baglio and A. Djouadi, *J. High Energy Phys.* **03** (2011) 055.
- [46] S. Chatrchyan *et al.* (CMS Collaboration), *Eur. Phys. J. C* **73**, 2469 (2013).
- [47] G. Aad *et al.* (ATLAS Collaboration), Reports No. ATLAS-CONF-2012-168 and ATLAS-COM-CONF-2012-203.
- [48] S. L. Glashow and S. Weinberg, *Phys. Rev. D* **15**, 1958 (1977).
- [49] G. C. Branco, P. M. Ferreira, L. Lavoura, M. N. Rebelo, M. Sher, and J. P. Silva, *Phys. Rep.* **516**, 1 (2012).
- [50] A. Djouadi, *Phys. Rep.* **459**, 1 (2008).
- [51] G. Aad *et al.* (ATLAS Collaboration), *J. High Energy Phys.* **11** (2014) 056.
- [52] G. Cacciapaglia, A. Deandrea, L. Panizzi, N. Gaur, D. Harada, and Y. Okada, *J. High Energy Phys.* **03** (2012) 070.
- [53] S. Dawson and E. Furlan, *Phys. Rev. D* **86**, 015021 (2012).
- [54] S. Alekhin, A. Djouadi, and S. Moch, *Phys. Lett. B* **716**, 214 (2012).
- [55] ATLAS and CMS Collaborations, Report No. ATLAS-CONF-2015-044.
- [56] K. A. Olive *et al.* (Particle Data Group Collaboration), *Chin. Phys. C* **38**, 090001 (2014).
- [57] G. Aad *et al.* (ATLAS Collaboration), Report No. ATLAS-CONF-2015-081.
- [58] CMS Collaboration, Report No. CMS-PAS-EXO-15-004.
- [59] J. F. Gunion, H. E. Haber, G. L. Kane, and S. Dawson, *The Higgs Hunter's Guide*, Frontiers in Physics Vol. 80 (Addison-Wesley, Reading, MA, 2000).